Eindhoven University of Technology
University Centre in Svalbard

Calibration of a Hyper Spectral Imager

Longyearbyen, December 2, 2019

Supervisor UNIS: Fred Sigernes
Supervisor TU/e: Hjalmar Mulders (EPG)

C.M. van Hazendonk 0912136

Abstract

The Hyperspectral Small Satellite (SmallSat) for Ocean Observation (HYPSO) mission aims to understand the effects of climate change and human impact on the world's ecosystem. Several targets such as potential harmful algae in front of the Norwegian coast will be studied using a compact, low-cost Hyper Spectral Imager (HSI) on board of the SmallSat. The HSI records a broad wavelength range scanning all wavelengths simultaneously, making it possible to identify algae underneath the water surface using post-processing. In order for the HYPSO mission to succeed, an optimal functioning of the HSI is essential. To fulfill its main purpose, identification of various targets, the HSI needs to be calibrated and characterized accurately. In this project, wavelength and radiometric calibrations are performed as well as characterizations of the bandpass, gain function, temporal linearity of the sensor and second-order diffraction effects. Ultimately, this project delivers a proof of functionality that shows that the HSI is able to identify targets and thus is ready for use in the HYPSO project.

Acknowledgement

Foremost, I would like to express my gratitude to Fred Sigernes, for providing the Hyper Spectral Imager (HSI) and introducing me to the field of hyperspectral imaging by sharing his extensive knowledge on the subject. Furthermore, I am grateful for his patience, enthusiasm and involvement in the project. The possibility to ask questions and the fact that he implemented the obtained results directly in the "PlaySpectrogram" program contributed a lot to the progress made in this project.

Furthermore, I would like to thank Marie Bøe Henrikson, who worked on the calibration of several HSI devices for her Master thesis. I learned a lot by studying her work and following the calibration and characterization procedures as described in her work.

Finally, I would like to give a special thanks to Hjalmar Mulders, my supervisor from Eindhoven University of Technology. Without him, I would not even have known that it is possible to study in Svalbard. Therefore, thank you very much for getting me into contact with Fred Sigernes and supervising me during the project itself.

Contents

List of abbreviations

CCD	Charged-Coupled Device
CMOS	Complementary Metal Oxide Semiconductor
dB	decibel
ENVI	Environment for Visualizing Images
FOV	Field of View
FPS	Frames per Second
FWHM	Full Width at Half Maximum
HSI	Hyper Spectral Imager
HYPSO	Hyperspectral Smallsat for Ocean Observation
NIR	near-infrared
NTNU	Norwegian University of Science and Technology
RGB	Red Green Blue
SmallSat	small satellite
SNR	signal-to-noise ratio
SWIR	shortwave infrared
UNIS	University Centre in Svalbard
UV	ultraviolet
VIS	visible

1 Introduction

A Norwegian research mission to protect the oceans, the Hyperspectral Small Satellite (SmallSat) for Ocean Observation (HYPSO) mission aims to understand the effects of climate change and human impact on the world's ecosystem [1, 2, 3]. It is lead by the Norwegian University of Science and Technology (NTNU) SmallSat Lab. For the mission, a SmallSat weighing only 3 kg is developed by NTNU in Trondheim to reduce costs and development time compared to traditional Earth-Observation satellites. The key feature of the SmallSat is a Hyper Spectral Imager (HSI) which registers a broader range of wavelengths than the human eye can see. This camera has the possibility to provide a high spatial resolution within a small Field of View (FOV), scanning a 50 km wide area. Post-processing makes it possible to identify targets in the recorded area invisible to the human eye or regular cameras. The satellite will observe the ocean along the Norwegian coast and the coast line itself, with a main focus on the detection of ocean color to target harmful algae, phytoplanton, river plumes and oil spill among others. Furthermore, a key motivation for this mission is to investigate the effects of climate change and human impact on the world's ecosystem. Using a HSI, it is possible to identify anthropogenic objects such as oil leaks and plastics using their spectral signatures. In addition, the behaviour of natural objects such as algae can give more insight in the way climate change affects the ocean and coast.

In order for the HYPSO mission to succeed, an optimal functioning of the HSI is essential. To fulfill its main purpose, identification of various targets, the HSI needs to be calibrated and characterized accurately. In this project, calibrations and characterizations will be performed to deliver a device ready for use in the HYSPO mission. To be able to do this, the topic of hyperspectral imaging needs to be understood.

Hyper Spectral Imaging or imaging spectroscopy combines the fields of imaging and spectroscopy, thus providing both spectral and spatial information at the same time. This is accomplished by not just recording an R, G and B coordinate per pixel, but a complete spectrum for each pixel in an image. So instead of having only spatial (x, y) information in the image, the color spectra for each pixel provide a third spectral (λ) dimension. In this way, a three-dimensional (x, y, λ) hyperspectral data cube is collected. The difference between a data cube of an RGB image and a hyperspectral data cube is the number of recorded spectral bands for each pixel. Instead of three bands, this becomes tens to several hundreds of bands for hyperspectral imaging such that the spectral band is continuous and thus every wavelength within the spectrum is covered [4, 5]. Depending on the application of hyperspectral imaging, the collected wavelength range can be chosen in ultraviolet (UV), visible (VIS), near-infrared (NIR) or shortwave infrared (SWIR) region [6].

The power of hyperspectral imaging lies in the high precision of the spectral information that is recorded at the same time. This makes it possible to identify various materials. Identification is also possible when the signals of different substances partially overlap in one image. Intervening atmosphere can for example be characterized in order to remove it from the obtained image [7]. Other advantages of hyperspectral imaging include the possibility to use spectral databases in combination with correlation techniques to improve the signal-to-noise (SNR) ratio of the data by the square root of the number of bands that has been used [7]. Together these advantages make hyperspectral imaging suitable for applications in remote sensing of the Earth, food safety, agriculture and biomedicine among others [5, 6, 7, 8]. Hyperspectral imaging techniques are especially suitable to detect vegetation, specific terrain features or man-made materials in nature [6].

This detection is based on the fact that all Earth's materials have a different spectral signature, meaning that a different part of the electromagnetic spectrum is reflected by the materials. As an example, the spectral responses of soil, vegetation and water are shown in figure 1.1. Using the spectral signatures, the various materials present in the remotely sensed images can be identified. For example it is possible to locate water resources or heavy metals and active mining areas [8]. Not only is it possible to detect and distinguish various types of materials, slight changes in the materials themselves are detectable as well. For instance the presence of suspended sediments or algae in water is visible due to a shift in the spectral response compared to regular water [8].

The use of hyperspectral imaging for remote sensing applications remote sensing started in the 1980s. In 2009, A. F. H. Goetz [7] published an extensive review about the first three decades of hyperspectral imaging. One of the first studies using hyperspectral imaging, reported in 1984, was conducted by

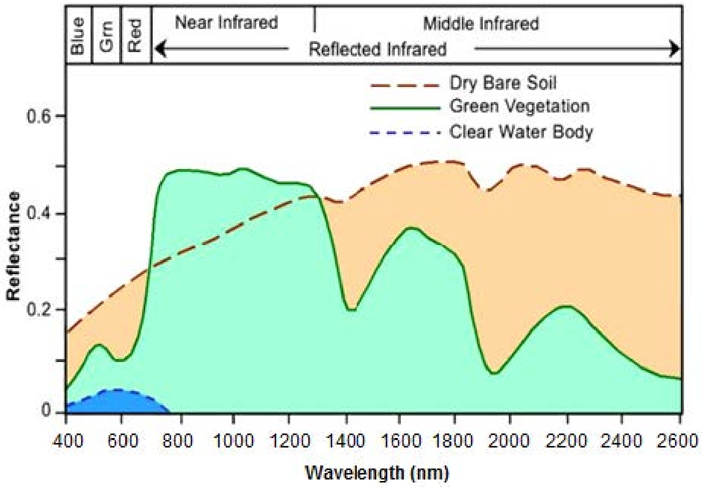

Figure 1.1: Spectral response curves of water, vegetation and soil. Figure retrieved from [8].

G. Vane *et al.* [9], using an airborn imaging spectrometer consisting of an 32 x 32 array detector which was able to measure 128 bands simultaneously ranging from 1.2 - 2.4 µm. For the measurements the pushbroom scanning technique was used, in which targets are scanned along the way perpendicularly to the entrance slit of the imaging device. A more detailed explanation of this technique will be given in section 2.2.1. Using the pushbroom scanning method, G. Vane *et al.* was able to scan materials and identify them afterwards as being the minerals aluite and kaolinite [7]. During the rest of the 1980s and the start of the 1990s, hyperspectral imaging was further developed for satellite remote sensing purposes. In this way it was used for various purposes such as target detection, environmental monitoring, geological search and analysis and monitoring of the atmosphere composition [6, 8]. One of the challenges arising with the development of more advanced hyperspectral imaging devices was the processing software needed for the handling of the large amount of obtained data. As an example, in 1989 no commercially available software packages could handle more than 10 spectral bands [7]. It was around this time that Joe Boardman and Kathryn Kierein-Young, two PhD students at the University of Colorado came up with the idea of storing the data in a hyperspectral data cube. Their data cube is illustrated in figure 1.2. Ultimately this lead to the development of the software package ENVI (Environment for Visualizing

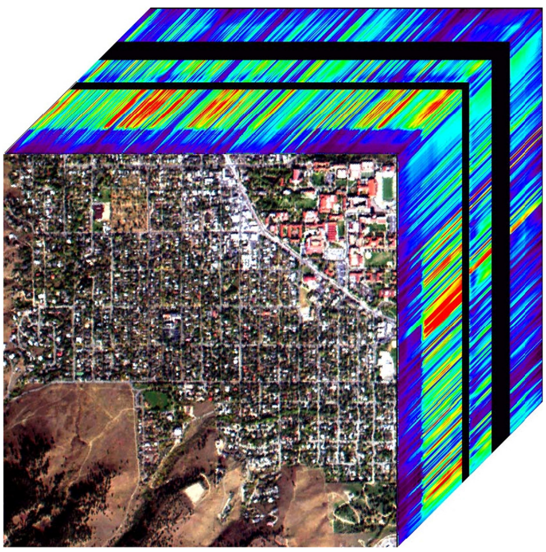

Figure 1.2: Representation of an hyperspectral imaging data cube as invented by Joe Boardman and Kathryn Kierein-Young. The colors represent the reflectance of the pixels. Image retrieved from [7].

Images) in 1994 by Joe Boardman, Fred Kruse and others which allowed the broader scientific community to process hyperspectral data as well, leading to an increase in the number of papers on hyperspectral imaging [7].

Besides the increase in knowledge of hyperspectral imaging, recent developments in CMOS (Complementary Metal Oxide Semiconductor) image sensors and 3D printing have given new opportunities to construct a low-cost HSI [10]. In this project, a low-cost and low-mass HSI, the pushbroom HSI v6, will be calibrated and characterized to get the device ready for use on the HYPSO mission. The device has been assembled by Fred Sigernes, professor of the University Centre in Svalbard (UNIS) using only off-the-shelf optical elements, mechanical parts and electronics. To fit the various parts together, a 3D printer is used. In this way, it is possible to make hyperspectral imaging accessible to projects with a tight budget, such as student projects or the HYPSO project.

In this study, the calibration and characterization of the HSI device is the main focus. M. Bøe Henrikson, a former master student at NTNU, has paved the way by setting up standard calibration procedures and describing several characteristics of HSI devices in her master thesis [11]. This project continues the work of M. Bøe Henrikson. More specifically, the aim of the project is to obtain the spectral response of the HSI v6, so that it can be incorporated in the data processing program "PlaySpectrogram" written by Fred Sigernes to enable the correct processing of the data recorded by the device. Lessons learned in this project will be incorporated into the design for the HYPSO mission to study the Earth from above and make it possible to identify various types of vegetation, algae and man-made objects present on the land and in the ocean. Ultimately, the goal is to get the HSI ready for use in the HYPSO project.

In this report, Chapter 2 covers the most essential theory which includes a basic background in spectroscopy as well as hyperspectral imaging in general. Subsequently, the necessary theory for calibrating and characterizing a HSI will be explained. The methods and the calibration results are given in Chapter 3. This includes an extensive overview of the HSI v6 as well as all the specific calibration and characterization methods. To illustrate the possibilities and strengths of the HSI v6 and to give a proof of functionality, some sample images taken outside of UNIS are shown in Chapter 4. In the end, the final conclusions regarding the calibration of the HSI v6 are presented in Chapter 5 followed by further optimizations of the HSI and an outlook in Chapter 6.

2 Theory

To explain the calibration procedures, basic knowledge of hperspectral imaging is needed. An introduction to spectroscopy will be given in section 2.1 after which hyperspectral imaging will be addressed in section 2.2. In this section both the pushbroom technique which is used in this project as well as the data processing are discussed. Subsequently, section 2.3 treats the relevant information concerning the calibration, after which section 2.4 describes characteristics that are important for the spectral signature of a HSI device.

2.1 Introduction to Spectroscopy

In imaging optics, a digital image is created by the imaging system. To understand its working principle, it is important to know the characteristic properties of light and the behaviour of light with respect to spectroscopy. Furthermore, this knowledge can help to explain abnormalities in the final outcome of the imaging system as well as compensate for these. Therefore, first the basic properties of light will be explained after which the relevant optical elements in an HSI and their behaviour will be explained.

2.1.1 Behaviour of Light

Light can be treated as both a particle and a wave, which is called the wave-particle duality. It means that light can be seen as a stream of photons behaving together as an electromagnetic wave. The wave can be described by

$$E(x,t) = E_0 \sin(\boldsymbol{k} \cdot \boldsymbol{r} \pm \omega t), \tag{2.1}$$

in which $E(x,t)$ is the amplitude of the wave and E_0 its maximum amplitude. The wave is periodical in time t and after $T = \lambda/v$, in which λ is the wavelength and v is the speed of light, the wave repeats itself. $\boldsymbol{k}$ is the propagation number which is related to the wavelength according to $\boldsymbol{k} = 2\pi/\lambda$. Furthermore, ω is the angular frequency and can be expressed as $\omega = 2\pi/T$ as well. Additionally, $\boldsymbol{r}$ is the position of the wave. It is also possible to write the wave equation in its complex form

$$\boldsymbol{E}(\boldsymbol{r},t) = \boldsymbol{E_0} \exp(i\phi), \tag{2.2}$$

in which ϕ the phase which can be written as $\phi = \boldsymbol{k} \cdot \boldsymbol{r} - \omega t + \zeta$ with the initial phase of the wave ζ.

To get a basic understanding of light waves going through an optical system, Gaussian optics can be used. Gaussian optics is based on the paraxial approximation which is the assumption that light propagates rectilinearly along the light rays. The direction of light waves is only altered by refraction and reflection. This is true in the approximation that the angle between the light ray and the optical axis is sufficiently small and therefore that the sine or tangent can be approximated by the angle itself [12].

To describe the direction of a light wave, the concept of a wavefront is used. The wavefront is defined as the surface along which ϕ remains constant. Using the definition of ϕ, the wavefront is located where $\boldsymbol{k} \cdot \mathbf{r}$ is constant for a plane wave. In general, $\boldsymbol{k}$ is oriented perpendicular to the wavefront. When using Gaussian optics, a ray is defined as normal to the wavefront meaning perpendicular to $\boldsymbol{k}$ [12].

Reflection and Refraction

Reflection and refraction of light is illustrated in figure 2.1. Reflection obeys

$$\theta_i = \theta_r \tag{2.3}$$

and refraction of light is described by Snell's law,

$$n_i \sin(\theta_i) = n_t \sin(\theta_t), \tag{2.4}$$

in which n_i and n_t are the refractive indices of media of the incident and transmitted light and θ_i and θ_t are their corresponding angles. In case of the paraxial approximation, equation 2.4 thus becomes

$$n_i\theta_i = n_t\theta_t \tag{2.5}$$

which is called the linearized Snell's law. However, when the rays are non-paraxial, this linearization does not hold and higher orders must be taken into account when expanding the sin function. This leads to aberrations such as distortion, coma, astigmatism and spherical aberration. Spatial and spectral distortion will be discussed in more detail in subsection 2.4.4.

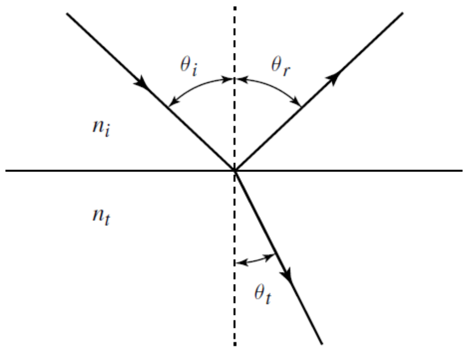

Figure 2.1: Refraction and reflection of light at the interface of to media with refractive index n_i and n_t. Figure retrieved from [12].

Diffraction and Interference

When light encounters different media, light waves can be altered by diffraction, leading to a direction change of the light wave due to an obstacle. Diffraction is only appreciable when the dimensions of the obstacle are comparable to those of the light wave. It can be seen in figure 2.2. On the other hand, interference takes place when multiple light sources are combined. The individual light waves will interfere with each other leading to an interference pattern with bright and dark spots, which is shown in figure 2.2 as well. The maxima of the interference pattern meet the requirement

$$n\lambda = a\sin(\beta), \tag{2.6}$$

in which n is an integer representing the spectral order, a is the distance between the two light sources and β is the angle between the path and a line from the source to the interference pattern. In total, an interference pattern caused by different apertures will be a combination of diffraction from the single apertures combined with interference between the different sources.

Reflectance, Transmittance and Absorptance

Besides diffraction and interference, light can undergo other processes. Reflectance describes the amount of light reflected by a surface, while transmittance gives the fraction of light passing a substance. Both processes can be described by the reflection and transmission coefficients respectively.

While passing a substance, part of the light is absorbed. Absorptance describes the rate of decrease of the light intensity when it passes a substance. It should be noted that absorbance, which describes the absorbance of light, is a different quantity than absorptance.

2.1.2 Important Definitions

In optics, many slightly different quantities are used with different units. To be able to distinguish those, their definitions and units are given in this subsection.

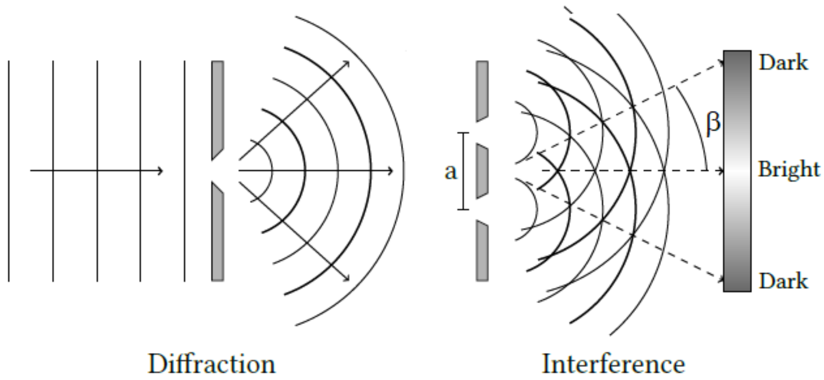

Figure 2.2: An example of diffraction of light due to an obstacle and interference between two light sources and its corresponding interference pattern. The distance between two light sources, a, and the diffraction angle, β, are shown in the figure. The figure has been adapted from [11].

Solid Angle

The definition of the solid angle, Ω, which is expressed in the unit steradians [sr], is

$$\Omega = \frac{A}{r^2} \tag{2.7}$$

in which A is the spherical surface area and r is the radius of the sphere. A schematical representation of this definition is shown in figure 2.3.

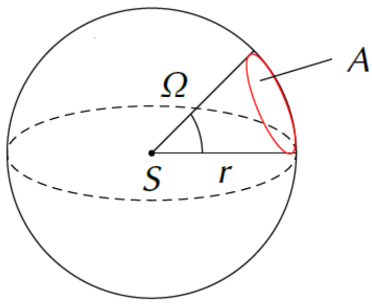

Figure 2.3: A schematic representation of the definition of the solid angle, Ω. S represents a source point, r the radius of the sphere and A the spherical surface area. Illustration from [11].

Flux

The flux Φ is defined as the number of photons or radiant energy emitted from a source S per unit of time. This leads to

$$[\Phi] = \frac{\#\text{ photons}}{\text{s}} = \text{W}. \tag{2.8}$$

Intensity

The intensity I of a source is coupled to a flux, but now the definition is changed into per unit solid angle. Thus the intensity is defined as the flux per unit solid angle, leading to the units

$$[I] = \frac{\#\text{ photons}}{\text{sr} \cdot \text{s}} = \frac{\text{W}}{\text{sr}}. \tag{2.9}$$

Radiance

To obtain the radiance from the intensity, the surface area is taken into account as well. This makes the definition of radiance the photon flux per unit area and solid angle, resulting in the units

$$[B] = \frac{\#\ \text{photons}}{\text{m}^2 \cdot \text{sr} \cdot \text{s}} = \frac{\text{W}}{\text{m}^2\text{sr}}. \tag{2.10}$$

Etendue

The etendue (geometrical extent), G of a system describes the ability of a system to accept light. It can be visualized by an acceptance cone or the FOV which described where photons are allowed to travel and thus determines how much light can be accepted by a detector. As an example the etendue of a front lens is displayed in figure 2.4. Here it can be seen that the etendue depends on the object distance p and the solid angle Ω where the light propagates into or out of. This leads to the following definition for the etendue

$$G = \int\int dS d\Omega\ [\text{m}^2\text{sr}] \tag{2.11}$$

in which S represents the are of an emitting source and Ω is the solid angle. When integrating equation 2.11, in this case it is allowed to obtain $G = S \cdot \Omega$. When using equation 2.7, Ω becomes

$$\Omega = \frac{A}{r^2} = \frac{\pi(r\sin(\Omega))^2}{r^2} = \pi\sin^2(\Omega). \tag{2.12}$$

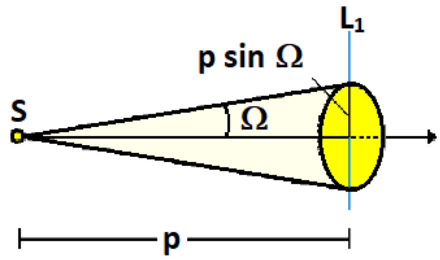

Figure 2.4: The etendue of the front lens. S represents the light source, p the object distance, L_1 the front lens and Ω the solid angle the light where photons are allowed to travel. Figure based on a figure from [13].

Since etendue represents the maximum geometric cone that an instrument can accept, it can be combined with the radiance to find the flux. Therefore, a new definition of flux as a function of radiance and etendue will be

$$\Phi = B \cdot G. \tag{2.13}$$

Using this formula, the photon flux in and out of a spectrometer can be calculated.

2.1.3 System Optics

Optical Diagram

In an optical diagram the path of the light through all the optical elements of a spectrometer is shown. An example is shown in figure 2.5. In this example a light source, three lenses, an entrance slit, a dispersive element and a sensor are used.

First the light from the source reaches the front lens with object distance p which focuses the light on the entrance slit. The image distance of the front lens is equal to q. The purpose of the entrance slit is to provide coherence by limiting the range of angles entering the dispersive element [12]. The slit has

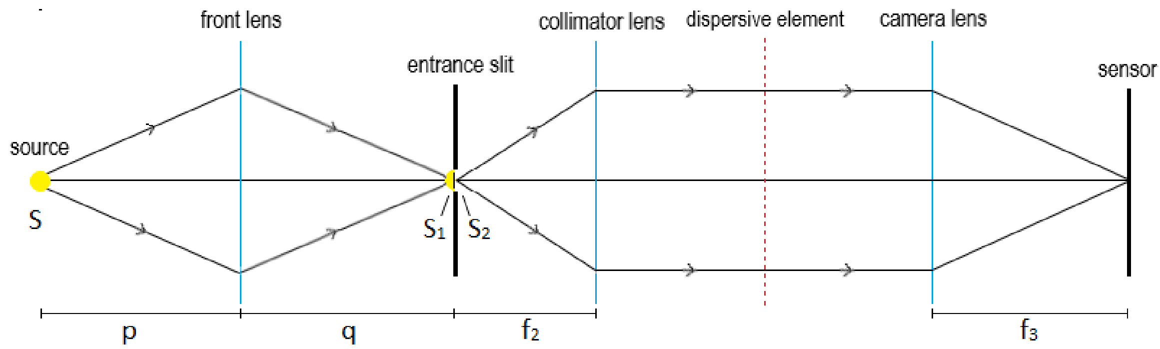

Figure 2.5: An example of an optical diagram consisting of a source, a front lens, an entrance slit, a collimator lens, a grating, a camera lens and a sensor. S is the source area, S_1 is the area of the source image, S_2 the area of the entrance slit. Furthermore, p is the distance between the object and the front lens, q the distance between the front lens and the entrance slit while f_2 and f_3 represent the distance between respectively the entrance slit and the collimator lens and between the camera lens and the sensor. In the center of the optical diagram, the optical axis is shown.

a typical width, w, combined with a height, h, regulating the inlet of light through the area S_2 of the slit.

After the entrance slit, the light falls onto the collimator lens which collimates the light before it reaches the dispersive element which can be a grating or a prism. The dispersive element splits the incoming light based on different wavelengths. The center wavelength will appear in the middle parallel to the optical axis. Subsequently, the light will fall onto the camera lens which focuses the light onto the sensor, which in turn converts the light into a spectrogram. The spectrogram contains spatial information on one axis and spectral information on the other. f_2 and f_3 are respectively the entrance arm lengths of the collimator lens and the exit arm length of the camera lens.

The lenses depicted in the optical diagram obey the thin lens formula

$$\frac{1}{f_1} = \frac{1}{p} + \frac{1}{q} \tag{2.14}$$

in which f_1 is the focal length, p the object distance and q the image distance.

Furthermore, it is possible to define the f/value of a lens also known as the speed of a lens. This value is described by the ratio between the focal length and the effective aperture. This result in the formula

$$f/\# \equiv \frac{f}{D} \tag{2.15}$$

in which f gives the focal length and D the effective aperture of the lens. High $f/\#$ numbers indicate a smaller effective aperture making it harder for light to pass through the lens and thus resulting in a smaller area of light illuminating the lens. This is illustrated in figure 2.6.

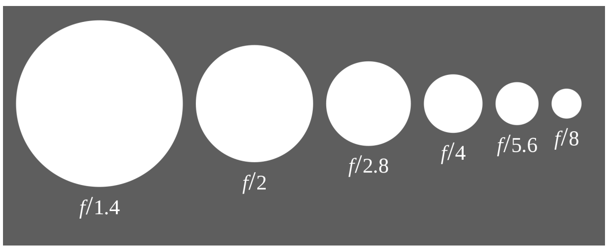

Figure 2.6: Apertures corresponding to different f/values. Figure retrieved from [14].

To maximize the etendue in the optical diagram, it should be kept constant through the different optical components. Therefore, the etendue is the same seen from both the entrance and the exit slit of an optical system. This means that the input etendue is equal to the output etendue of a spectrometer, described by

$$G = \pi S \sin^2(\Omega) = \pi S_1 \sin^2(\Omega_1) = \pi S_2 \sin^2(\Omega_2), \tag{2.16}$$

in which S_1 is the source of the entrance slit, S_2 is the image of the exit slit, Ω_1 is the etendue of the entrance slit (input etendue) and Ω_2 is the etendue of the exit slit or the spectrometer (output etendue). The etendue depends on the grating equation, the size of the used slits and the different optical elements.

Grating

The key optical element of a HSI is the dispersive element which can be either a grating or a prism or a combination (GRISM) of both. The purpose of this element is the dispersion of incoming light to split the different wavelengths. There are two different types of gratings, a transmitting grating and a reflective grating. The first diffracts the light while transmitting it, while the second uses reflection of the light with the help of different mirrors for diffraction. In the end, both gratings will result in the same interference pattern.

A diffraction grating consists of N grooves. The spacing between the grooves is equal to a and each groove has a width b. In a grating, each groove acts as a single wave source and thus together all grooves form a diffraction and interference pattern following the interference theory. All wavelengths are diffracted to the same spot for the 0^{th} spectral order which is indicated by the diffraction angle β. However, for higher spectral orders the diffraction angle is wavelength dependent. Lower wavelengths such as blue light will have a smaller value for β than longer wavelengths. When instead of a grating a prism is used, the opposite effect will take place. In a prism the lower wavelengths are diffracted the most while the longer wavelengths are diffracted less. Since prisms and gratings work opposite, a dispersive element combining both (GRISM) will make sure that the light goes straighter through the design.

The separation of wavelengths is essential for HSI devices based on gratings, since various wavelengths will be detected at different spots of the detector. This immediately leads to the fact that the efficiency of a grating is slightly altered for different wavelengths. Therefore, a grating within the correct wavelength range should be chosen.

To get the grating equation of a diffraction grating, equation 2.6 which describes the interference of light waves is slightly altered to include the incident angle as well. It becomes

$$n\lambda = a(\sin(\beta) \pm \sin(\alpha)) \tag{2.17}$$

in which α represents the incident angle and β the diffracted angle of the grating. For a reflective grating, equation 2.17 is used with a plus sign, while for a transmission grating, the minus sign is applicable.

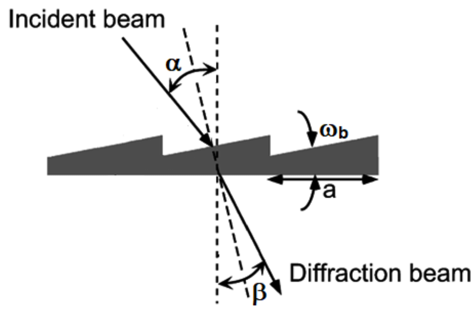

Figure 2.7: The working principle of a blazed transmission grating. a is the distance between two grooves, α the angle of incidence, β the diffraction angle and ω_b the blaze angle. The figure has been adapted from [15]

A special type of diffraction grating is a blazed diffraction grating, which is shown in figure 2.7. It optimizes the maximum efficiency for a specific refraction order losing as little as possible to other spectral orders. The optimization is achieved by introducing a blaze angle ω_b. Due to ω_b the most efficient angle for the grating is reached when

$$\alpha - \omega_b = \omega_b - \beta. \tag{2.18}$$

When combining equation 2.17 and 2.18, the blaze wavelength is given by

$$\lambda_b = \frac{2a}{n} \sin(\omega_b) \cos(\alpha - \omega_b) \tag{2.19}$$

for a reflective blazed grating and

$$\lambda_b = \frac{2a}{n} (\sin(\alpha) + \sin(\alpha - 2\omega_b)) \tag{2.20}$$

for a transmission blazed grating. The blaze wavelength corresponds with the wavelength for which the efficiency of the grating is the highest. Therefore, it can also be called the peak wavelength [16].

Bandpass

The bandpass of a system describes the distance over which adjacent lines can be separated. It is defined as the recorded Full Width at Half Maximum (FWHM) of a monochromatic spectral line. An example of the line width of a monochromatic line and the bandpass of a well aligned an real instrument are shown in figure 2.8.

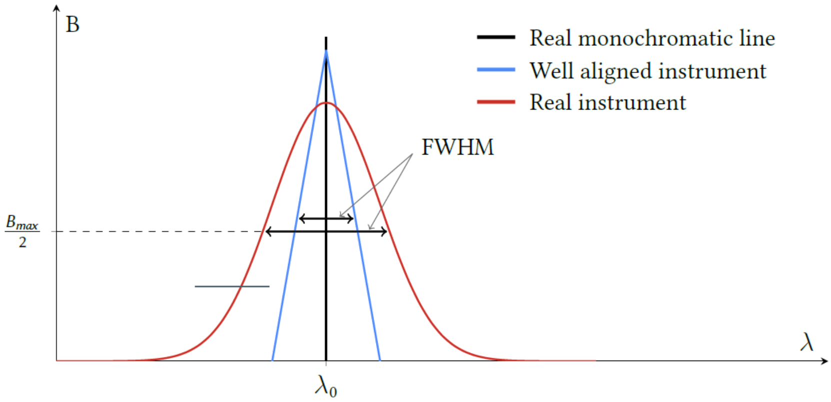

Figure 2.8: A schematic representation of the real width of a monochromatic line, the FWHM of a real instrument and that of a well aligned instrument. Illustration retrieved from [13].

The bandpass can be calculated using

$$\text{BP} = \text{FWHM} \approx \frac{d\lambda}{dx} \times w' \quad [\text{nm}] \tag{2.21}$$

in which $\frac{d\lambda}{dx}$ represents the linear dispersion and w' the width of the exit slit. The linear dispersion describes the spread in wavelength per sensor distance. The exit slit width can be seen as the image of the entrance slit as a function of wavelength. Due to the correlation between the entrance and the exit slit, it is also possible to describe the bandpass in the entrance slit width. Equation 2.21 then becomes

$$\text{BP} = (\frac{a \cos \alpha}{n f_2}) \times w. \tag{2.22}$$

a is the distance between two grooves in the grating, α is incident angle, n the spectral order, f_2 the focal length of the collimator lens and w is the entrance slit width.

Sensor Detection and Quantum Efficiency

The sensor on which the image is focused converts the irradiance (photons) into an electrical signal. To be able to do this, an array consisting of detectors and a multiplexer are necessary. First the array of detectors collects the incoming photons and converts it to an electronic response. Afterwards the multiplexer collects this electronic response and converts all the signals from the individual detectors into one signal with a digital representation of the collected image. Multiplexers are usually a Charged-Coupled Device (CCD) or a CMOS switching circuit. CMOS sensors are cheaper, but more noisy at the same time because more circuitry is needed within each unit cell.

When a sensor converts the irradiance into an electrical signal, some of the signal gets lost. The quantum efficiency describes the spectral response of each individual pixel in the detector array and thus quantifies how many electrons are produced by the sensor as a fraction of the number of photons that reach each pixel. It should be noted that the quantum efficiency is wavelength dependent.

2.2 Hyper Spectral Imaging

Hyperspectral imaging records images over a broad wavelength range, thus capturing hyperspectral data cubes consisting of one spectral and two spatial dimensions. The device used for recording the images is called a HSI and can be based on different designs of which most have a dispersive element as key optical element. Post-processing of the hyperspectral data cubes makes it possible to extract information and identify targets invisible to the human eye.

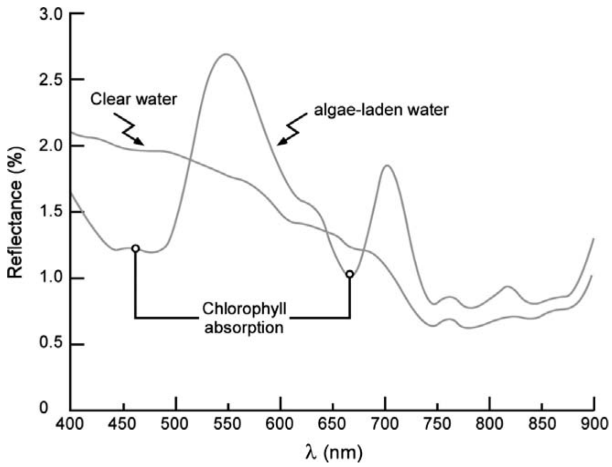

Figure 2.9: The spectral response of clear water and water with algae. In the response curve of water with algae, absorption peaks due to the chlorophyll are visible. Figure adapted from [17].

An example of what could be made possible using post-processing are algae located just below the water surface and thus invisible to the human eye. However, since these algae contain chlorophyll, the spectral characteristics of water with algae underneath changes, as can be seen in figure 2.9. The changes are occurring due to absorption of light by the chlorophyll molecules. Using these changes, the algae can made visible in post-processing. As an example how this could look like, an image of Miffy (Dutch: Nijntje) in an inflatable pool is shown. When only looking at the an RGB version of this image in figure 2.10, no algae are visible. In figure 2.11 a hyperspectral image of the same setting is shown. Here post-processing has been used to make the algae in the water visible. In this way, post-processing can be used to for example identify algae after recording hyperspectral datacubes of water.

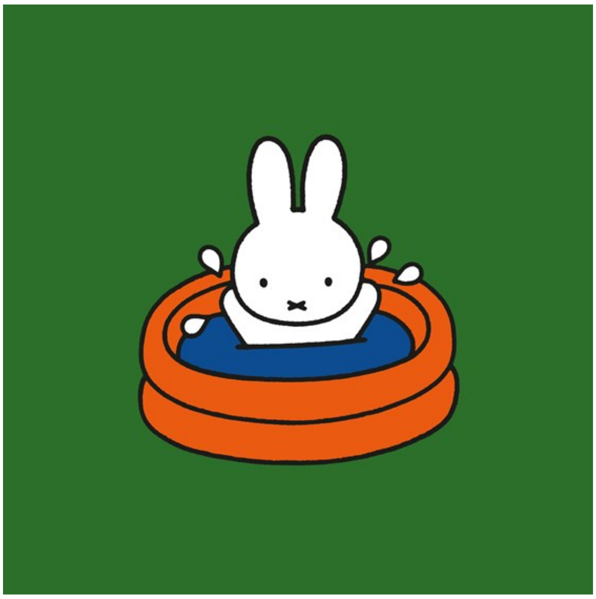

Figure 2.10: Example of the information visible with an RGB image. Image retrieved from [18].

Figure 2.11: An example of the extra information that can be made visible when post-processing a hyperspectral datacube. Image adapted from [18].

2.2.1 Pushbroom Technique

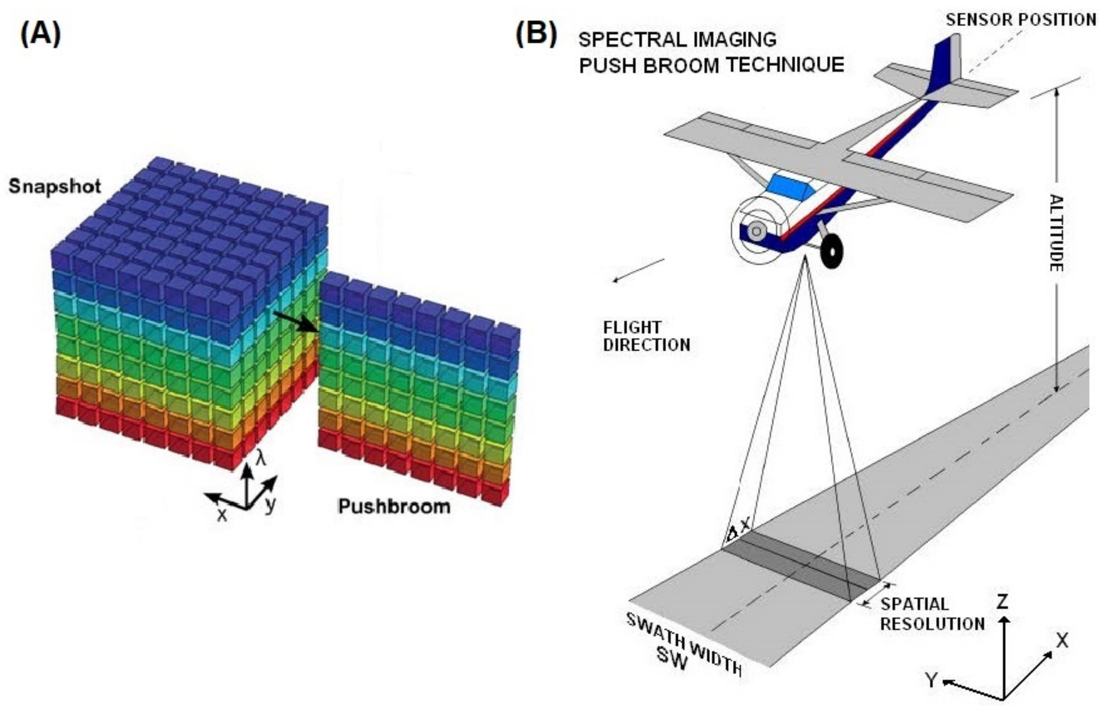

Figure 2.12: (A) Schematic representation of the acquisition of a hyperspectral datacube using the pushbroom method. Figure adapted from [5]. (B) Illustration of the pushbroom technique by using an airplane to scan the flight direction (x). Image retrieved from [13].

In the pushbroom hyperspectral scanning technique, a 2D detector array collects one slice of the datacube containing one spatial (y) and one spectral (λ) dimension at the same time. The second spatial dimension

(x) has to be scanned. The scanning can for example be accomplished by mounting the HSI to an airplane to scan the area underneath with the optical slit oriented normal to the flight direction [13] or by attaching the HSI to a rotating table. A schematic representation of the datacube itself and the pushbroom scanning principle can be found in figures 2.12A and B. It is shown that the hypercube thus consists of two spatial and one spectral dimension.

The main advantage of the pushbroom scanning technique is that all the wavelengths are recorded at the same time. This makes it both a fast and an accurate technique, since no time deviations are included. Another advantage of the pushbroom scanning technique is its relative low complexity in combination with an acceptable SNR to be used in remote sensing application. However, it should be noted that the scanning method is not perfect, giving rise to distortions which make it more difficult to identify the various species.

2.2.2 Data Processing

As mentioned in section 2.2.1, the acquired data comes in the form of a 3D hyperspectral datacube with two spatial and one spectral dimension (x, y, λ) which is shown in figure 2.12A. The huge amount of data provides a challenge to extract the relevant information from this cube. An example of information that can be obtained is a spatial frame containing only the two spatial dimensions for a particular wavelength. When combining all these spatial frames into one image, each pixel in this image will consist of a point spectrum describing the intensity for all different wavelengths.

By combining three of these spatial frames (one red, one green and one blue) it is possible to construct an RGB image. In this way the wavelengths of interest to detect for example algae, plants or plastics can be chosen.

2.3 Calibration

When recording data with a HSI, the information is usually stored as number of counts per pixel. To convert this into more meaningful units, calibration is essential. In calibration, a known standard is compared to the data obtained by a specific instrument to enable this conversion of units. In case of hyperspectral imaging devices, a wavelength calibration and a radiometric calibration should be performed in the lab. The latter assumes the wavelength calibration to be known [19]. For the use of hyperspectral imaging in remote sensing application, a calibration in-flight is also beneficial, because the spectral response parameters of the sensor may change due to vibrations, temperature and pressure changes when operating in flight compared to the laboratory environment [20]. The in-flight calibration will not be treated in this report.

2.3.1 Wavelength Calibration

Wavelength calibration or spectral calibration provides a relation between the pixel and the wavelength. A basic method to perform the calibration uses several spectral lamps with known peaks in the wavelength range of the detector. The spectral lamps illuminate a diffuse screen to ensure a uniform illumination of the FOV. Subsequently, a HSI records calibration images of the spectrum projected on the diffuse screen after which the measured peaks are related to the known wavelengths providing a relationship between the two.

2.3.2 Radiometric Calibration

To identify the relation between the electronic counts as a function of the number of incident photons on the instrument, radiometric calibration also known as sensitivity calibration is necessary. This type of calibration determines the throughput, the usable photon flux at the detector sensor, in units of radiance or reflectance instead of in digital counts. The throughput depends on the input flux, the geometrical extent, the efficiency and quality of the optical elements in the HSI and the conversion of photons into electronic counts at the detector [21].

While both the efficiency of the optical elements and the throughput can be determined theoretically, radiometric calibration provides a more practical solution to find the total throughput. Radiometric calibration is performed using a reference source with known intensity and spectral characteristics. This source is used to illuminate a diffuse reflective screen, which is recorded by the HSI. The diffuse screen is essential since it ensures that the entire FOV of the HSI is illuminated uniformly [21].

Besides providing a relation between the raw number of electronic counts and the radiance, radiometric calibration is capable of compensating or removing deviations of the hyperspectral sensor [11]. The goal of radiometric calibration is to find the calibration factor K for the individual pixels. K can be determined using

$$K_\lambda = \frac{M_\lambda}{C} \left[\frac{\text{mW}}{\text{m}^2 \text{ sr nm counts}}\right] \tag{2.23}$$

in which M_λ represents the radiant existance of the screen and C the background corrected sensor counts per second of the radiometric lamp [21].

The radiant existance M_λ of a diffusive screen gives its brightness as observed by an instrument. It can be calculated using

$$M_\lambda = B_{o\lambda}\rho_\lambda \left(\frac{z_0}{z}\right)^2 \cdot \cos(\alpha) \left[\frac{\text{mW}}{\text{m}^2 \ \ \text{nm}}\right], \tag{2.24}$$

in which $B_{0\lambda}$ is known radiance from a calibration lamp, ρ_λ represents the reflectance factor of the screen for each specific wavelength and α the angle between the the lamp and the screen.

To determine C, the dark current, b_0, should be subtracted from the raw detector count. The dark current is defined as the number of detected counts by the sensor without any illumination. Causes of dark current can be thermal excitation or leakage currents for example.

Data obtained by the radiometric calibration can also be used to determine the temporal linearity of the sensor and the effect of different gain values on the output of the sensor. Ideally, the sensor would show a linear response when exposed to different exposure times. If some non-linearities are found, these should be corrected before the actual radiometric calibration can take place [22]. More theory about the influence of gain and the temporal linearity of the sensor can be found in subsections 2.4.1 and 2.4.2 respectively.

2.4 Characterization

2.4.1 Gain Function

In electronics, gain is used to increase the power of the input signal in order to get a higher output signal. This increase in signal is established by adding additional energy to the signal. Gain is usually expressed in the logarithmic unit decibel (dB). In hyperspectral imaging gain can be used to get a brighter image when taking images of dark environments or it can compensate for low exposure times. Since gain is expressed in logarithmic units, the standard formula for power gain is

$$\text{gain} = 10 \cdot \log_{10}\left(\frac{P_{\text{out}}}{P_{\text{in}}}\right) [\text{dB}][23] \tag{2.25}$$

in which P_{out} is the power from the output and P_{in} is the power applied to the input. When rewriting this equation to the voltage or current gain, the expressions $P = V^2/R$ and $P = I^2R$ are used respectively. Under the assumption that $R_{\text{out}} = R_{\text{in}}$, which can be made since the intensity is proportional to the square of the amplitude in optics, this leads to

$$\text{gain} = 20 \cdot \log_{10}\left(\frac{V_{\text{out}}}{V_{\text{in}}}\right) = 20 \cdot \log_{10}\left(\frac{I_{\text{out}}}{I_{\text{in}}}\right) [\text{dB}] \tag{2.26}$$

in which V_{out} is the voltage from the output, V_{in} is the voltage applied to the input, I_{out} is the current from the output and I_{in} is the current applied to the input. In hyperspectral imaging, the output signal is recorded in number of counts which is proportional to the electrical current. When rewriting these formulas to predict the output signal in hyperspectral imaging for a specific gain, the formula

$$\text{counts}_{\text{detected}} = \text{counts}_{\text{gain }0} \cdot 10^{\text{gain}/20} \tag{2.27}$$

is obtained. This equation makes it possible to use a gain higher than zero during dark or fast measurements and process the data as if a value of zero gain was used.

2.4.2 Temporal Linearity of the Sensor

An ideal detector would have a temporal linear sensor response, meaning that the number of counts scales linearly with the exposure time. However, if the sensor does not show a linear response, this should be compensated for. The sensor response is linear when the uncertainties of the measurement are larger than the non-linearities in the sensor response [11].

2.4.3 Second-Order Diffraction

When a diffraction grating is used, the wavelengths are diffracted multiple times, resulting in multiple spectral orders. This means that photons of one wavelength can be found at multiple wavelengths. If a broad wavelength range is used, overlap between spectral orders can appear. To understand this overlap and the exact spectral position of each diffraction order, the grating equation as given by equation 2.17 should be studied in more detail.

This equation can be simplified when an incident angle of zero degrees is used. When taking into account $\alpha = 0$ in the setup, this leads to the equation

$$\lambda = \frac{a}{n}\sin(\beta) \tag{2.28}$$

in which a is the spacing between the grooves of the grating, n is the order of refraction and β is the diffracted angle of the grating.

Equation 2.28 shows that second-order refracted photons appear at twice their initial wavelength. So for light with an initial wavelength of 400 nm, its second-order refraction will occur at 800 nm. So if a wavelength range of for example 400 - 1000 nm is used, the number of photons counted between 800 - 1000 nm will consist of both first-order diffracted photons with a wavelength of 800 - 1000 nm and the second-order diffracted photons of 400 - 500 nm. Therefore, to obtain the correct number of first-order diffracted photons, the measured value should be compensated for the second (and higher) order diffracted photons.

2.4.4 Spectral and Spatial Distortions

In hyperspectral imaging, often spectral and spatial misregistrations occur, caused by for example aberrations and alignment errors between the optical elements, leading to non-physical phenomena occurring in the spectral signatures of the images. A consequence of the distortions is that the emission lines in a hyperspectral image frame no longer follow the grid lines but can be bent.

An important spectral distortion is the keystone error, in which the same spatial pixel of an image changes position as a function of wavelength, making the spectrogram looked skewed. A typical spectral distortion is smile, the change of the central wavelength in a spectral channel as a function of slit height, resulting in the bending of the emission lines in the spectrogram. Both effects are shown in figure 2.13.

For the final calibration, both effects should be compensated for to obtain a higher resolution of the final image. This correction currently falls beyond the scope of this project, but is a recommended future addition. Therefore, to avoid most spatial and spectral distortions in the rest of the calibration, the centerline has been used to determine all calibration parameters. However, this means that the calibration might be less accurate for other pixel positions.

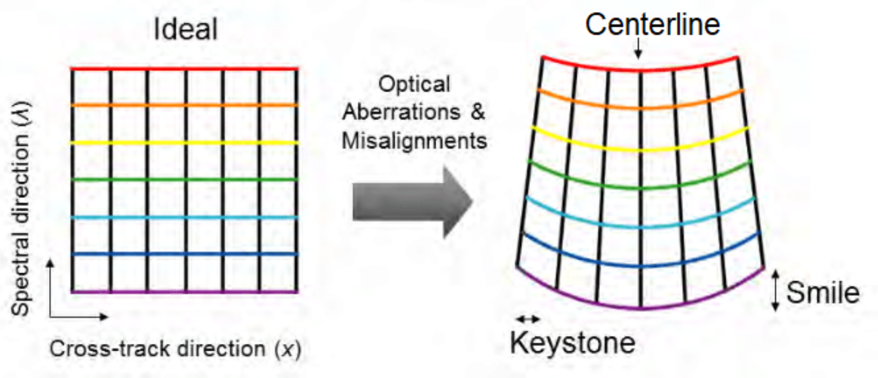

Figure 2.13: Left an ideal hyperspectral frame is shown, on the right, keystone and smile errors are illustrated. Figure inspired on [24].

3 Methods and Results

In this chapter, the imaging equipment as well as the calibration and characterisation procedures will be explained. Subsequently, the corresponding results for each calibration step will be given. Furthermore, the characteristics of the Hyper Spectral Imager version 6 (HSI v6), which has been used in this project, will be discussed.

3.1 Pushbroom HSI v6

The HSI v6 has been built by Fred Sigernes at UNIS and is described in [25]. However, a few components, such as the imaging source detector and the entrance slit, have been changed compared to [25].

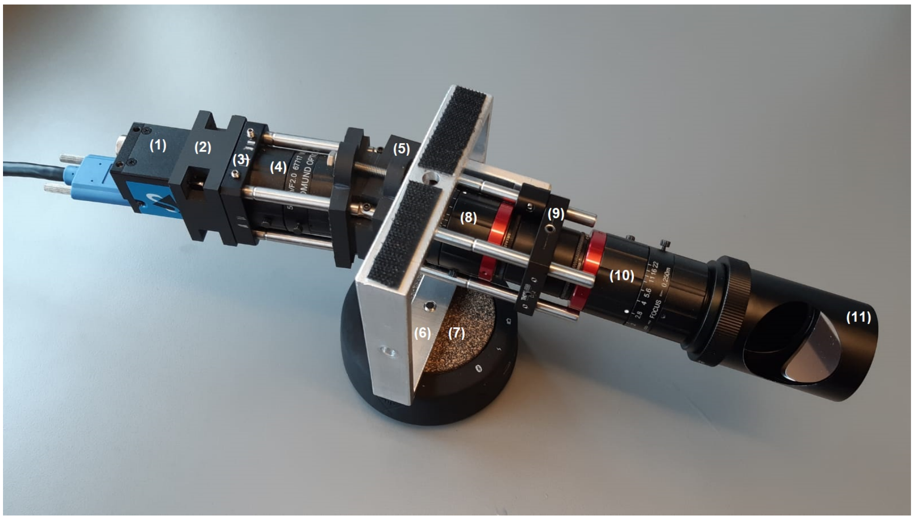

Figure 3.1: Pushbroom HSI v6 with (1) DMK 33UX174 camera head, (2) 3D printed camera mount insert, (3) CP12 cage plate, (4) camera lens, (5) 3D printed grating holder with grating (300 lines/mm), (6) aluminum holder, (7) motion control system, (8) collimator lens, (9) CP12 cage plate, (10) front lens and (11) 37 mm 45° mirror.

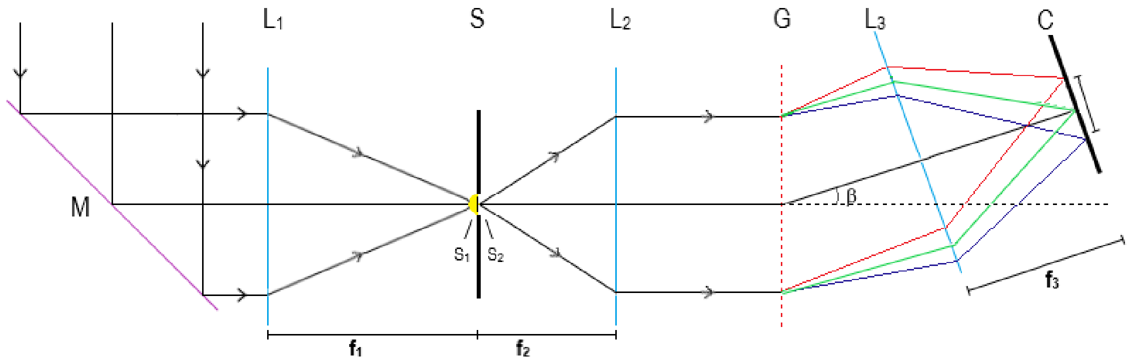

Figure 3.2: Optical diagram of the HSI v6. The light comes in via de mirror (M) after which it is reflected to the frond lens (L_1). Subsequently, it is focused onto the entrance slit (S) and passes to the collimator lens (L_2) which focuses the light on the transmission grating (G). The grating diffracts the light with a diffraction angle $\beta = 10.37°$ for the center design wavelength $\lambda = 600$ nm. Finally, the camera lens (L_3) directs the light to the camera head (C) where the photons are collected.

In figure 3.1 the assembled pushbroom HSI v6 device is shown and in figure 3.2 the corresponding optical diagram is depicted. Specifications of the individual parts and the complete device can be found in table 1. During this project, the mirror mounted at the entrance of the HSI has partly been removed for calibration purposes.

The grating that has been used in the design, is a blazed grating with a blaze angle of 17.5°. Its efficiency as a function of wavelength can be found in Appendix B. To regulate the coherence of the light that falls onto the transmission grating, an entrance slit with a height of 7 mm and a width of 50 μm has been mounted in between the front lens and the collimator lens in the lens tube as seen underneath part (9) in figure 3.1. It should be noted that these lenses are designed for 2/3" sized detectors with a maximum usable image size of $6.6 \cdot 8.8$ mm^2. Therefore, the entrance slit height is 0.4 mm too high. This should be compensated for during the data processing to ensure that only the certified image circle of the lenses is used to prevent additional aberrations in smile and keystone. This compensation is accomplished by removing the upper and bottom 31 pixels corresponding to parts of the image produced by the upper and bottom 0.2 mm of the entrance slit.

Another feature of the lenses that should be taken into account is their working distance. The quality of the images produced by the lenses is only guarantied within a range from 250 mm to infinity. Images taken within 250 mm of the front lens could suffer from aberrations and should not be used.

Item	**Specifications**
Camera head	DMK 33UX174 USB 3.0 monochrome industrial camera with 1/1.2 inch Sony CMOS Pregius sensor (IMX174LLJ)
Camera lens	Edmund Optics #67717 lens 50 mm/F2.0 VIS-NIR
Transmission grating	Edmund Optics #49579 transmission diffraction grating 300 lines/mm), 25.0 mm^2 17.5°, blazed transparent
Collimator lens	Edmund Optics #67717 lens 50 mm/F2.8 VIS-NIR
Entrance slit	Thorlabs height 7 nm, width 50 μm
Front lens	Edmund Optics #67717 lens 50 mm/F2.8 VIS-NIR
Mirror	Bower 37 mm mirror scope compact right angle
Image size	(1080, 1920)
Spectral range	Approximately 270 - 1000 nm
FWHM	3.3 nm (theoretical)
Rotating system	Syrp Genie mini motion control system

Table 1: Specifications of HSI v6.

3.1.1 Data Collection and Processing Software

For the data collection of the HSI the program IC Capture 2.4 (version 2.4.642.2631) has been used. This program shows the image recorded by the HSI and has the possibility to record images or movies. Images and videos are recorded in 8-bit unsigned integer arrays (uint8) leading to a maximum recorded intensity of $2^8 - 1 = 255$ counts. Furthermore, the program enables to change settings of the HSI detector such as exposure time and gain. The exposure time can be set from $1/5000 - 30.0$ seconds and the gain range is from $0 - 48$ dB.

For the data processing both the program PlaySpectrogram developed by Fred Sigernes and Matlab were used. The program PlaySpectrogram allows to transform videos recorded by the HSI into images for a desired wavelength. Furthermore, it provides the possibility to see the point spectrum of each pixel. Next to this program, Matlab has been used to write the codes to process the data and for example identify calibration parameters such as the spectral bandpass, the spectral range and the calibration coefficients. In the end, the data obtained by data processing in Matlab has been used to optimize the PlaySpectrogram program.

3.2 Calibration

It should be noted that not all parts of the calibration worked out well the first time they were performed. During the process, several errors in the calibration process have been discovered and resolved. These errors as well as some calibration related advice is written in Appendix A to make the process easier for future students.

For both the wavelength and the radiometric calibration, a diffusive screen, Spectralon (SRT-99-180) is used. The screen is from Labsphere, Inc. with a reflectance factor of approximately $\rho_\lambda = 0.98$ in the visible and near infrared regions of the spectrum. The exact factors can be found in table 2.

Wavelength (nm)	**Reflectance factor**
400.0	0.984
450.0	0.984
500.0 - 850.0	0.986

Table 2: Reflectance factors at an angle of 8 degrees normal to the screen for the SRT-99-180 screen in the relevant wavelength range [21],

3.2.1 Wavelength Calibration

For the wavelength calibration, a hydrogen vapour tube (Edmund Optics Ltd. SN K60-906) and a Mercury (Hg) vapour tube (Edmund Optics Ltd. SN K60-908) with known emission peaks have been used in combination with a diffuse screen. These peaks with their corresponding wavelengths are depicted in table 3.

The characteristics of these tubes have been measured with the HSI v6 with zero gain and no binning. To avoid measurement errors, the average pixel values for each peak from a dataset of 45 images have been used. In order to avoid the influence of spectral and spatial misregistrations such as smile and keystone for the pixel wavelength correlation, the data of the pixels in the central row has been used. From now on, this data will be referred to as the centerline. The average spectral pixel values are shown in table 3 as well and the average centerline is plotted in figure 3.3. It should be noted that the Mercury peak located at 404.7 nm has not been used for the wavelength calibration, due to the low signal of this peak. Additionally, the double Sodium peak at 577/579.1 nm has only been used as check afterwards, since this peak consists of two peaks.

Emission	**Wavelength (nm)**	**Pixel position**
Hg (k=1)	404.7	-
Hg (k=1)	435.8	415.4 ± 0.6
H_β	486.1	545.1 ± 0.5
Hg (k=1)	546.1	700.7 ± 0.5
Na	577/579.1	-
H_α	656.3	987.0 ± 0.1
Hg (k=2)	809.4	1395.4 ± 0.9

Table 3: The reference peaks for the Mercury vapour tube and the hydrogen vapour tube (line H_β and H_α of the Balmer series) as well as the average spectral pixel values that have been measured during the calibration.

With the known emission peaks and the measured spectral pixel values, the pixel wavelength correlation can be deduced by using a second-order polynomial fit

$$\lambda \approx a_0 + a_1 \cdot [px] + a_2 \cdot [px]^2 \tag{3.1}$$

in which λ is the wavelength in nanometers, px the measured spectral pixel index and a_0, a_1 and a_2 are constants [13, 21]. Using the measured pixel values from table 3, their values are $a_0 = 271.6 \pm 0.8$,

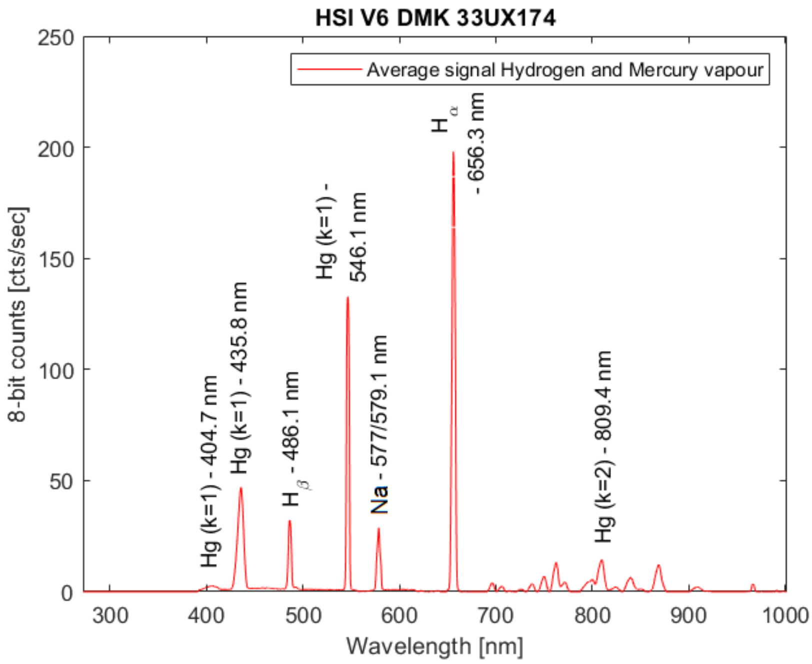

Figure 3.3: The wavelength calibration of HSI *v6. The shown spectrum represents an average of 45 calibration images taken with zero gain and no binning. The spectra are produced by the illumination of a Hydrogen and Mercury (Hg) vapour tube on a diffuse screen.*

$a_1 = 0.399 \pm 0.002$ and $a_2 = -1.0 \pm 0.1 \cdot 10^{-5}$, corresponding to a spectral range from $271.6 - 1001.8$ nm. While obtaining these constants, a pixel count starting at zero has been used instead of a pixel count starting at one. The location of the double Na-peak with these constants is found at 578.5 nm which is indeed within the range of the two peaks located at 577 and 579.1 nm.

It should be noted that not the entire spectral range of the HSI can be used, because this range covers the entire spectral axis without taking into account the spectral ranges of the optical elements in the device. In principle the optical design is optimized for wavelengths in the range 400 - 800 nm. Below 400 nm, the efficiencies of both the lenses and the transmission grating drop rapidly. For example in case of the grating the absolute efficiency drops from 40% at 400 nm to a value of approximately 5% for 300 nm as can be seen in figure B.1 in Appendix B. Therefore, wavelengths below 400 nm cannot be used. For wavelengths above 800 nm, the efficiency of the grating drops from 50% at 800 nm to a bit over 30% for 1000 nm. Additionally, the spectral response curve of the sensor present in the camera head, the Sony IMX174LL, shows a relative response below 25% for wavelengths exceeding 900 nm as can be seen in figure B.2 in Appendix B. On top of the dropping efficiencies for higher wavelengths of the optical elements, the second-order diffraction effects start to play an important role above 800 nm. When looking at the grating equation, it is seen that the second-order diffraction of 400 - 500 nm is located in the range from 800 - 1000 nm. In order to use this wavelength range, it should be compensated for the second-order diffracted photons. To conclude, the spectral range from 400 - 800 nm can be used without problems, while wavelengths above 800 nm need to be compensated for second-order diffraction effects. Furthermore, below 400 nm and above 900 nm the efficiency of the optical elements becomes insufficient. Therefore only the wavelength range from 400 - 900 nm has been used in this project of which the part from 800 - 900 nm has been compensated for second-order diffraction effects.

Additionally, it can be seen that the standard deviation in the calibration parameters is relatively large. This arises due to the fact that the various calibration images have a variation of a few pixels for some of the emission peaks when comparing the 45 different calibration images. This variation could be caused by the limited bandwidth.

3.2.2 Radiometric Calibration

Dark Current

As explained in subsection 3.2.2 of the theory, it is expected to have a certain number of counts per pixel without any illumination. To know the value of the dark current and thus being able to compensate for it is essential. Therefore, the first part of the radiometric calibration procedure consists of taking the dark current spectra with zero gain and no binning. As a comparison these images have been taken at different exposure times to investigate the effect of exposure time on the dark current as well.

The mean value of a dark current image is calculated after which the average over all dark current images is taken. 11 images have been used to calculate this average value. With zero gain and no binning this leads to an average dark pixel count of 15.00125 ± 0.00007. It should be noted that this dark current value is independent of the exposure time and therefore it should not be scaled with the exposure time. This very low standard deviation is supported by plots of the dark current. The dark current of the centerline of all images are plotted in figure 3.4, while the dark current of an entire frame is plotted in figure 3.5. It can be seen in the plots that the dark current is almost constant at the value of 15 counts per pixel. In figure 3.5 a few brighter spots corresponding to values above 15 counts can be identified.

Since the centerline is used for most of the data processing and the determination of the constants and the dark current at the centerline shows a constant value of 15, a dark current of 15 counts is subtracted from the recorded data to compensate for the dark current.

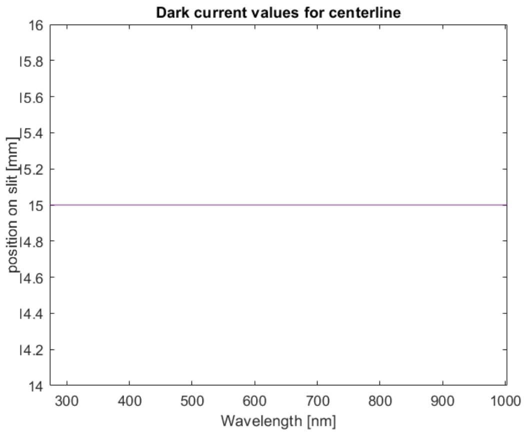

Figure 3.4: The intensity distribution of centerline of the dark current for the different dark current calibration images.

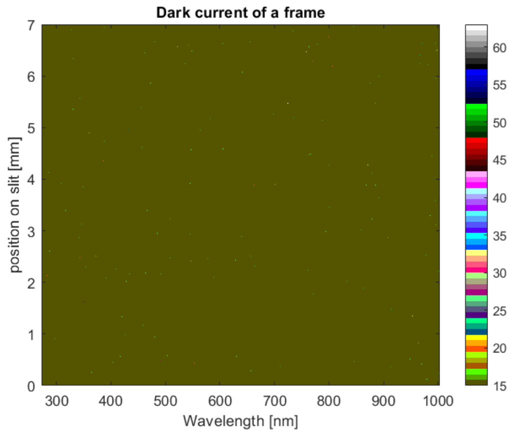

Figure 3.5: The intensity of the dark current for an entire image frame.

Radiometric Constant

In the second part of the radiometric calibration, the radiometric constant will be determined. For this determination a calibrated 1000W Tungsten lamp (Oriel SN7-1275, model number 63350) operated at 8.2 A and 110.6 V with a spectral range of 250 - 2400 nm has been used. The calibration of this lamp has been performed at 0.50 m. The calibration certificate of the lamp can be found in Appendix C. The spectral irradiance of this lamp can be found in table 4. It can be seen that the Tungsten lamp behaves as a black body radiator having its maximum irradiance around $\lambda_{\max} \approx 900$ nm, giving the lamp its deep orange and red glow. This peak irradiance corresponds to a black body temperature of approximately $T \approx 3200$ K when Wien's law, $\lambda_{\max} \cdot T = 2.8 \cdot 10^{-3}$ m K is used.

Since the certificate values of the Tungsten lamp are obtained at a different distance from the lamp, the values should be compensated. For this compensation, the fact that the lamp can be regarded as a point source, radiating photons isotropically is used. This implies that the total amount of photons passing through a sphere with radius z_0 should equal the amount of photons passing through a sphere with radius z. This yields

$$4\pi z_0^2 B_{0\lambda} = 4\pi z^2 B_{z\lambda}, \tag{3.2}$$

in which $B_{0\lambda}$ is the certificated radiance from the spectral lamp at distance z_0 and $B_{z\lambda}$ is the radiance that hits the screen at distance z. Rewriting this equation gives

$$B_{z\lambda} = B_{0\lambda} \cdot \left(\frac{z_0}{z}\right)^2 \left[\frac{\text{mW}}{\text{m}^2 \ \ \text{nm}}\right]. \tag{3.3}$$

Furthermore, to perform the calibration, the calibrated wavelength values of the Tungsten lamp should be interpolated for all wavelength values. For this interpolation different approaches are available.

Wavelength (nm)	**Spectral Irradiance (mW/(m^2 nm))**	**Spectral Irradiance (# photons/(cm^2 s nm))**
400.0	20.16	$4.060 \cdot 10^{11}$
450.0	37.31	$8.452 \cdot 10^{11}$
500.0	67.25	$1.693 \cdot 10^{12}$
555.0	99.45	$2.779 \cdot 10^{12}$
600.0	125.8	$3.800 \cdot 10^{12}$
654.6	153.3	$5.052 \cdot 10^{12}$
700.0	173.6	$6.117 \cdot 10^{12}$
800.0	205.7	$8.284 \cdot 10^{12}$

Table 4: Certificate spectral irradiance values of 1000 W Tunsten lamp model 63350 (ORIEL SN7-1275). These values are obtained at a nominal distance of $z_0 = 0.5$ m. The current through the filament is 8.2 A and the corresponding voltage is 110.6 V.

Huang *et al.* [26] found that an optimal fit of the certified calibration data could be obtained by using

$$B_\lambda \approx \lambda^{-5} \cdot \exp(c_0 - c_1\lambda^{-1}) \cdot \exp\left(c_2\lambda - c_3\left|\frac{\lambda - \lambda_0}{500}\right|^{c_4}\right) (\text{for}\lambda < \lambda_0) \tag{3.4}$$

and

$$B_\lambda \approx \lambda^{-5} \cdot \exp(c_0 - c_1\lambda^{-1}) \cdot \exp\left(c_2\lambda + c_5\left|\frac{\lambda - \lambda_0}{500}\right|^{c_6}\right) (\text{for}\lambda > \lambda_0). \tag{3.5}$$

In these equations, c_i are the fitting parameters of which c_3 and c_5 should be positive and $\lambda_0 = 450$ nm. Both the method provided by NIST and the improved methods, should be fitted separately for low wavelengths ($\lambda < 450$ nm) and higher wavelengths ($\lambda > 450$ nm). It can be seen that the first part of both equations is similar, $\lambda^{-5} \cdot \exp(c_0 - c_1\lambda^{-1})$. This part of the equation describes the Planck's law for black-body emission. The second part of both equations approximates the lamp emissivity. When performing the interpolation of the Tungsten lamp, the values $46.3, -4967, -0.00230, 22.6, 401, 0.768$ and 1.18 have been found for $c_0, c_1, c_2, c_3, c_4, c_5$ and c_6 respectively.

When the interpolated values describing the radiance of the calibration lamp that hits the screen are known, the radiant existance of the screen M_λ should be determined by using equation 2.24. For this formula, the values of ρ_λ for different wavelengths can be found in table 2. Furthermore, the 1000 W Tungsten lamp has been located at distances of 1.20 m and 1.50 m from the diffusive screen under an angle $\alpha = 0$. Images with zero gain and no binning have been taken to determine the calibration coefficient K.

Finally, when M_λ is known, equation 2.23 can be used to determine the radiometric calibration factor K_λ. Since the number of counts per second can be different for all pixels of the calibration image, the calibration constant will be a matrix. This matrix will have the same size as the spectrogram and is shown in figure 3.6. For the lowest wavelengths, the number of counts in the radiometric calibration images is equal to zero. Hence, the radiometric constant K will be equal to infinity. These values are depicted in black. Furthermore, it can be seen that for the wavelength region 400 - 800 nm, the K values are mostly in between 0 and 0.2. To see the differences in K value more clearly, only the values in between 0 and 1 are depicted in figure 3.7. In this figure, the infinity values are still black and the values above 1 are red. The larger K values starting from 800 nm and in particular 900 nm, indicate that a larger correction needs to be made in this regions. This is necessary due to the poorer performance of the optical elements in this region. Therefore, relatively less photons reach the detector for these wavelengths, which makes the data in this wavelength range more noisy.

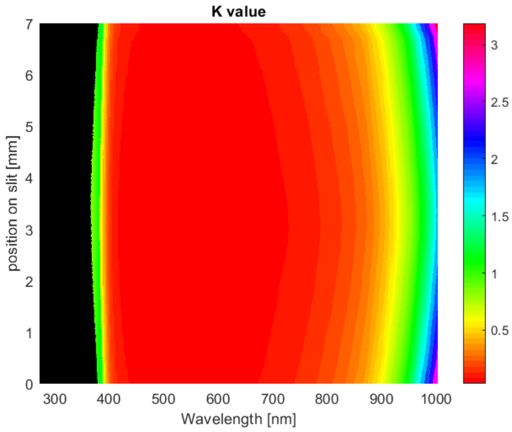

Figure 3.6: The K matrix for the entire detector size. The black parts represents areas without counts, therefore the K value is calculated to be infinity in these areas.

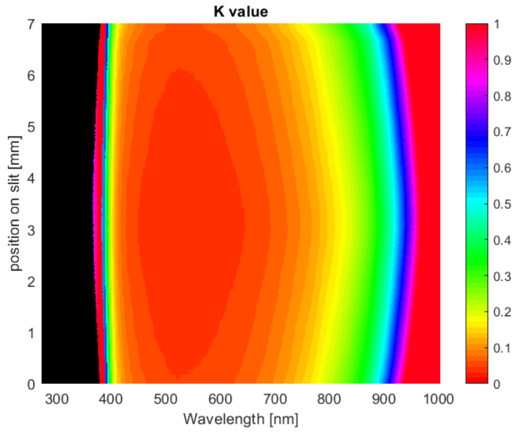

Figure 3.7: The K matrix for the entire detector size showing the K values from 0 to 1. Infinity values are represented by black and values above 1 by red.

In figure 3.8, the intensity of the Tungsten calibration lamp at 22.5 dB is plotted as a function of the wavelength. Furthermore, also the calibration values of the Tungsten lamp at a distance of 1.20 m from the lamp itself are calculated and plotted in the same graph. The calibration values are depicted in spectral radiance instead of in counts. When comparing the shape of the Tungsten lamp and the sensitivity of the HSI v6, it should be noticed that the Tungsten lamp is not the ideal radiometric calibration source. The maximum intensity for the Tungsten lamp is found at 900 nm, while the HSI v6 has its maximum intensity around 625 nm. This means that the Tungsten lamp emits a lot of red light, while the HSI v6 is more sensitive to light with lower wavelengths. Furthermore, the emission spectrum of the Tungsten lamp deviates a lot from that of the Sun, which is more prominent in the blue part of the spectrum. Therefore, the radiometric calibration might not be optimal for taking images outside with this specific device.

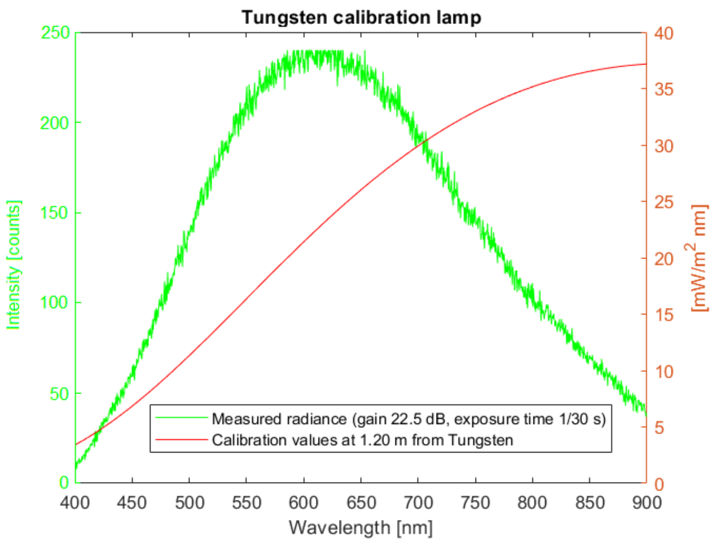

Figure 3.8: The intensity of the observed spectrum from the Tungsten lamp measured with gain 22.5 dB,an exposure time of 1/30 s and a distance of 1.20 m from the Tungsten lamp and the calibration values in $mW/(m^2nm)$ of the Tungsten lamp calculated for a distance of 1.20 m.

As a last step in the radiometric calibration, the temporal linearity of the detector and the influence of different gain factors are studied. The temporal linearity of the sensor is investigated by taking images with different exposure times, while the effect of gain was studied by increasing the gain while keeping a constant exposure time. In this way, the equation for gain as given in equation 2.27 can be verified. The results of these characterisation studies are given in subsections 3.3.2 and 3.3.3.

3.3 Characterization

To increase the understanding of the HSI, the spectral bandpass, gain function and exposure time function have been determined.

3.3.1 Spectral Bandpass

The bandpass of the HSI can both be determined theoretically and experimentally. For the theoretical bandpass, equation 2.22 is used. When using the values of the system, $a = 3.33 \cdot 10^{-6}$ m, $\omega = 50 \cdot 10^{-6}$ m, $f_2 = 50 \cdot 10^{-3}$ m and $\alpha = 0°$, the theoretical spectral bandpass for the system becomes 3.33 nm for the first spectral order.

To determine the spectral bandpass experimentally, the property that the spectral bandpass equals the FWHM of a peak is used. With Matlab the peaks are identified and their widths can be determined. Subsequently, the obtained pixel values can be converted into wavelength values to obtain the FWHM in nanometers. This is done for 45 calibration images, after which the average value and the standard deviation are determined.

The spectral bandpass is expected to be smallest close the the center wavelength of the device which is $\lambda = 600$ nm. Therefore, it is expected that the FWHM of the peaks closest to the center wavelength will be the smallest. So the FWHM of the 546.07 nm Argon and the 656.3 nm H_α peaks should be smallest. Since the 577/579.1 nm Hg ($k = 1$) peak consists of two separate peaks, this FWHM will probably be a bit larger.

The average FWHM for the different peaks when taking into account 45 calibration images are shown in table 5. The standard deviation of the FWHM of H_α is zero, since this FWHM for this peak was the same for all 45 calibration images. Combining all different peaks results in an average spectral bandpass of 4 ± 1 nm. When taking the standard deviation into account, it coincides with the theoretically expected value for the spectral bandpass, which is equal to 3.3 nm. Furthermore, it can be seen that the FWHM for the mercury peak at 546.1 nm is the smallest. It is even smaller than the theoretical bandpass. This could be caused by the fact that one pixel corresponds with a wavelength shift of approximately 0.39 nm, making the real standard deviation a bit larger than the standard deviation calculated when comparing the spectral bandpass of all 45 calibration images.

Emission	**Wavelength (nm)**	**FWHM (nm)**
Hg (k=1)	435.8	5.1 ± 0.3
H_β	486.1	3.44 ± 0.08
Hg (k=1)	546.1	3.1 ± 0.1
Hg (k=1)	577/579.1	4.1 ± 0.2
H_α	656.3	3.80
Hg (k=2)	809.4	5.6 ± 0.4

Table 5: The reference peaks for the Mercury vapour tube and the hydrogen vapour tube (line H_β and H_α of the Balmer series).

3.3.2 Gain Function

As described in section 2.4.1, it is expected that the output values for different gain values behave according to equation 2.27. To study the effect of gain, images at increasing gain values have been taken at an exposure time of 1/30 s. At gains higher than 22.5 dB, overexposure of the detector was seen and therefore this data has not been used. Furthermore, the dark current calibration has first been performed on the data before using it to find a relation for the number of counts as a function of gain.

In figure 3.9 the spectra of the centerline of the images taken at different gain values are shown. With the help of fitting each spectra, the maxima for all these spectra are determined. These maxima as a function of gain are plotted in figure 3.10 as well as the gain equation as given in equation 2.27. It can be seen that the theoretical relation as described by the theory holds well for the measured values of the maximum number of counts.

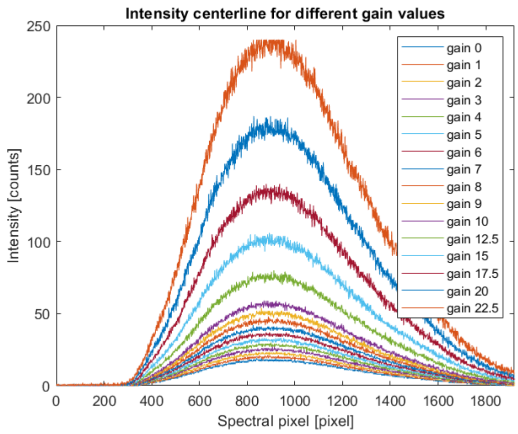

Figure 3.9: The recorded spectra of the centerline for increasing gain. The number of counts is shown as a function of the pixels.

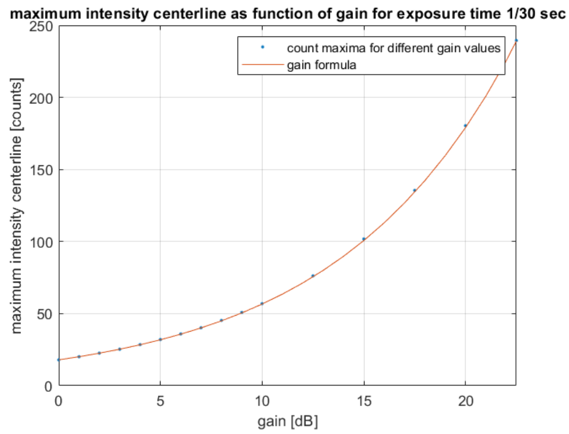

Figure 3.10: The maximum number of counts as a function of gain. The gain formula as described by equation 2.27 has been plotted through the data points.

3.3.3 Temporal Linearity of the Sensor

To investigate the temporal linearity of the sensor, the Tungsten lamp has been used. The Tungsten lamp has been placed at a distance of 9.81 m from the diffuse screen. Subsequently, the screen has been recorded by the HSI using different exposure times ranging from 1 to 20 s. The intensity of the centerline (after subtraction of the dark current) of the different images has been fitted with a nine degree polynomial fit with which the maximum intensity for each exposure time has been determined.

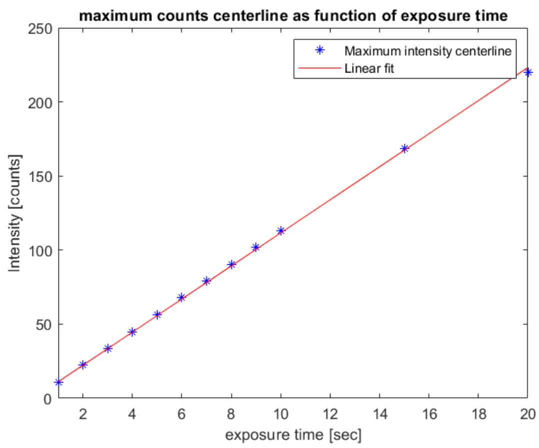

Figure 3.11: The maximum number of counts as a function of the exposure time. A linear fit of the data points has been performed resulting in $y = a \cdot x$ with $a = 11.16 \pm 0.09$.

Afterwards the maximum intensities are plotted as a function of the exposure time and a linear fit through the data points has been performed. Since a maximum intensity of zero is expected for an exposure time of zero seconds, the fitting formula $y = a \cdot x$ has been used. The result is shown in figure 3.11. The obtained fit is $a = 11.16 \pm 0.09$. Indeed it can be seen that the sensor response is approximately linear. Therefore, a linear sensor response is assumed in this report.

3.3.4 Second-Order Diffraction

When the values obtained by the fitting the raw spectrum of the Tungsten lamp are used to transform the intensity spectra [counts] of the hyperspectral images of the environment of UNIS into the irradiance spectra [mW/(m^{2}nm)], it can be seen that strange effects occur above 800 nm. Where a relatively low irradiance and a downward trend in the infrared range is expected, the values of the irradiance in this region increase. An example of this convertion is shown in images 3.12 and 3.13. The first image shows the intensity spectrum in counts, while the second image shows the irradiance of the same pixel. The pixel is part of the centerline of an image taken from the roof of UNIS.

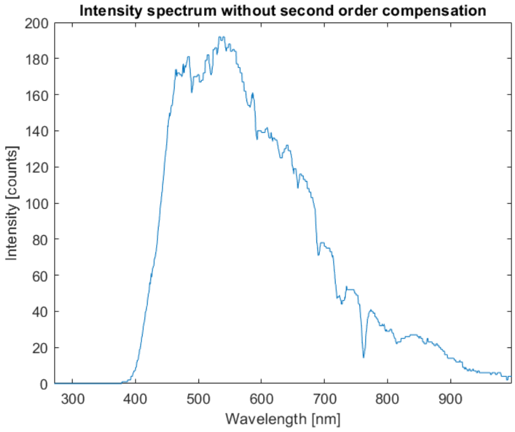

Figure 3.12: The intensity spectrum of a pixel from a sample image taken outside as obtained after the standard radiometric calibration without applying a second-order diffraction correction.

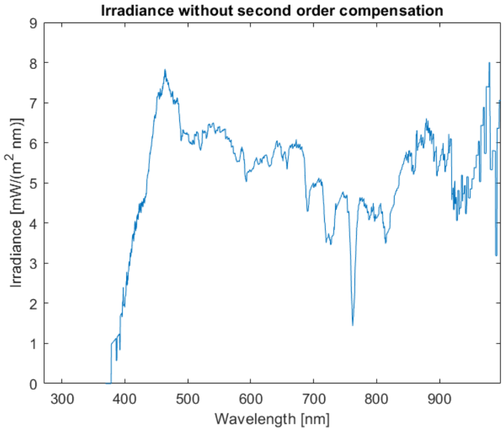

Figure 3.13: The irradiance spectrum of a pixel from a sample image taken outside as obtained after the standard radiometric calibration without applying a second-order diffraction correction.

Since the detector of the HSI v6 is capable of recording a spectral range from approximately 270 - 1000 nm, with sufficient efficiency of optical elements between 400 - 900 nm, effects caused by second-order diffraction will start to play an important role for higher wavelengths. For hyperspectral images recorded of the environment, the second-order diffraction effects play a much more prominent role than of the calibration images of the Tungsten lamp. This difference can be explained by the difference between the solar spectrum and the Tungsten spectrum. The blue part of the spectrum has an important contribution to the solar spectrum, while this part is almost absent in the Tungsten calibration lamp. This can be seen in the spectra plotted in figure 3.8.

However, the second-order diffraction effects of the HSI v6 in particular are caused by wavelengths in the range of 400 - 500 nm, because their second-order emission will occur around 800 - 1000 nm as described by equation 2.28. Therefore, a compensation should be applied to remove the second-order signal from the intensity count.

To remove the second-order signal, first the contribution of the second-order effect should be known. To get insight into this contribution, measurements using a cut-off filter have been performed. The goal of the cut-off filter is to block all wavelengths below 500 nm in order to avoid all second-order effects. The cut-off filter used for this experiment is the 2-63, having zero transmission below 575 nm as can be seen in the transmission graph of 2-63 in Appendix D. When the efficiency of the filter is taken into account and compensated for, the second-order contribution is clearly visible as can be seen in figure 3.14. The corresponding compensated irradiance spectra are shown in figure 3.15.

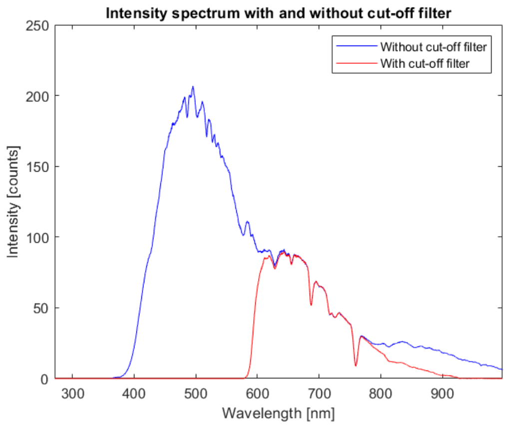

Figure 3.14: The intensity spectrum in counts measured with and without cut-off filter 2-63.

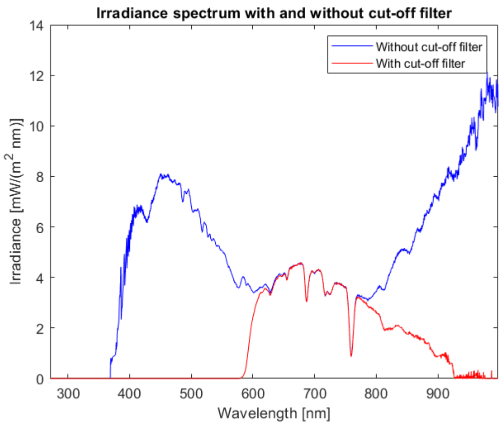

Figure 3.15: The irradiance spectrum measured with and without cut-off filter 2-63.

With the information shown in figure 3.14 it is possible to calculate the efficiency of the second-order diffraction for all wavelengths. Using this efficiency, all images can be second-order compensated. For this correction, the formula

$$C'_{800} = C_{400} \cdot A_{800} + C_{800} \tag{3.6}$$

in which C'_{800} represents the number of measured counts at 800 nm, C_{400} the number of counts at 400 nm, A_{800} is the efficiency of the second-order diffraction occuring at 800 nm and C_{800} is the number of counts at 800 nm without taking second-order diffraction into account, has been used. The equation can be extended to all different wavelengths from 780 - 1000 nm for which second-order effects play a role.

Applying equation 3.6 to the spectra shown in figure 3.12 and 3.13, the second-order compensated intensity and irradiance spectra are obtained. These new spectra are shown in figures 3.16 and 3.17. It should be noted that the second-order correction leads to some negative values of the intensity spectrum above 900 nm. Since a negative number of counts is physically impossible, these values have been set to zero counts.

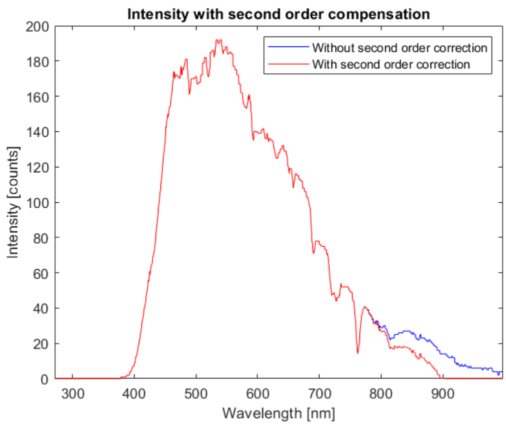

Figure 3.16: The intensity spectrum of a pixel after second-order compensation.

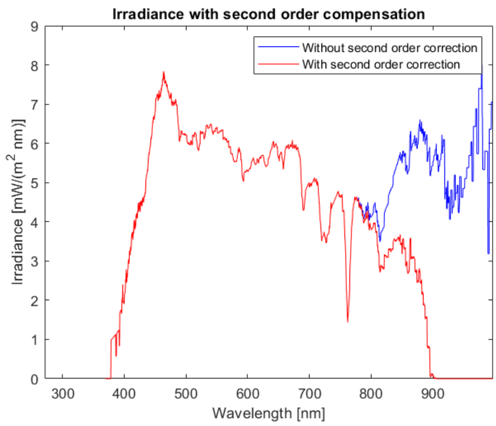

Figure 3.17: The irradiance spectrum of a pixel after second-order compensation.

4 Proof of Functionality

To proof the functionality of the HSI v6 and hyperspectral imaging in general, some test samples of the surroundings of UNIS have been taken. In this section, some of the information of these test videos is shown both as images and as point spectra.

In order to transform the recorded videos into images, several Matlab scripts have been used. The basic steps that have been taken for the conversion from video to image involve:

1. reading out the individual frames.
2. removing the parts of the frames corresponding to the upper and lower 0.2 mm of the entrance slit.
3. calculating the wavelength calibration for one of the frames to use this wavelength calibration for the entire video. Preferably a bright pixel representing snow or sky is used to have a higher resolution when performing the wavelength calibration.
4. removing the dark current from the intensity counts
5. applying the second-order wavelength correction to all frames.
6. applying the radiometric calibration to second-order corrected frames.
7. choosing a wavelength for the red, green and blue part as well as a bandpass for the final RGB image.
8. reading out the correct spectral pixels for the chosen wavelength for all calibrated frames.
9. scale the values for the red, green and blue channels for the RGB image so that the lowest value of one of the three channels is zero and the highest value of one of the channels becomes 255. It should be noted that not all channels should scale from 0 to 255, because the differences in intensity between the different channels could still exist.

After all these steps, the horizontal number of pixels of the created image is equal to the number of frames from the video, while the vertical number of pixels is equal to 1018.

Figure 4.1: A picture taken on the roof of UNIS *with a mobile phone camera on 26-08-19 13:12.*

The first hyperspectral data cube, which has a video format, that will be treated in this section, is the cube corresponding to the same view as the regular image 4.1. From now on, this data cube will be referred to as data cube K. To check the wavelength calibration, first the intensity spectrum of one frame is used to obtain the Fraunhofer lines. The Fraunhofer lines represent spectral absorption lines present in the spectrum of the Sun and are shown in figure 4.2. Especially with a blue sky, these lines are clearly visible. Since the Fraunhofer peaks always appear at the same wavelength, they are very suitable to use as spectral reference points.

To check the wavelength calibration of the video, a bright part of the centerline of the future image is used to have the highest possible resolution and to neglect possible aberrations when moving away from the centerline such as smile and keystone. In this image, the white boat visible in frame 2904 is used. This spectrum is shown in figure 4.3. The Fraunhofer lines which have been used for the spectral calibration are depicted in the image. When performing the spectral calibration the formula $\lambda \approx 267.6189 + 0.4004911 \cdot px - 1.080696 \cdot 10^{-5}$ is found for the pixel wavelength correlation.

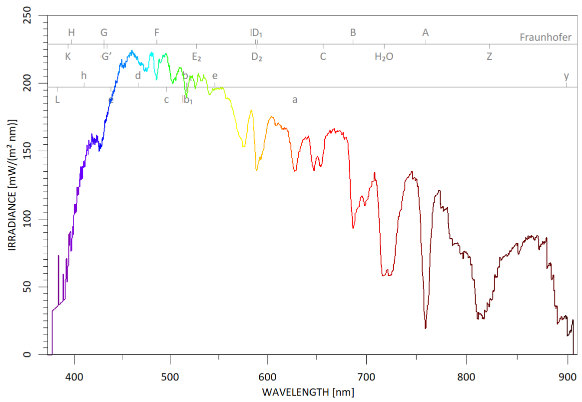

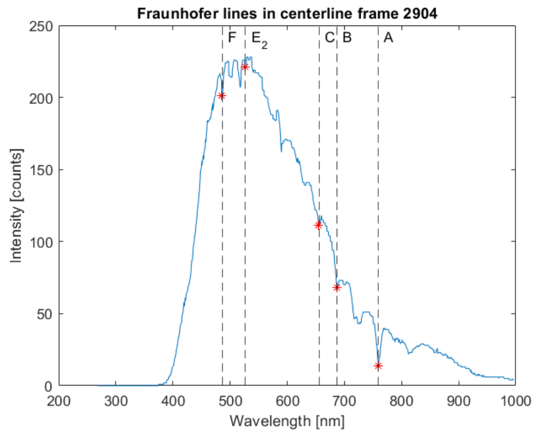

Figure 4.2: The Fraunhofer lines as visible in the sky during daylight. This image has been produced using the program PlaySpectrogram and a self recorded hyperspectral data cube.

Figure 4.3: The Fraunhofer lines in the intensity spectrum of the centerline of frame 2904 that have been used to perform the wavelength calibration.

After all the calibration steps, images from the hyperspectral data cube K can be generated, which results in for example figures 4.4 and 4.5. In figure 4.4 realistic wavelengths for the red, green and blue colors have been chosen, resulting in an image representing the mobile phone picture relatively well. On the other hand, in figure 4.5, the NIR wavelength 780 nm has been used for the red color. This change is mostly visible for the grass plants on the mountainside on the left side of the image, because grass plants contain chlorophyll. Chlorophyll absorbs strongly in blue (450 nm) and red (670 nm) and subsequently emits light in the NIR [8]. Using image 4.5, it is visible that grass has a relatively high irradiance in the NIR. This observation is supported by the Albedo irradiance spectra given for several different ground components by A. Filippo in his PhD thesis [27]. These spectra can be found in figure 4.6. When the irradiance spectrum of the grass part of data cube K is studied in more detail, the graph as shown in figure 4.7 is found. It can be seen that this irradiance is quite similar to that found by A. Filippo [27] in figure 4.6.

Figure 4.4: Image generated from hyperspectral datacube K recorded on 26-08-2019 13:14. The wavelengths used for the RGB image are: red 660 nm, green 540 nm and blue 480 nm.

The effect of the NIR irradiance of grass is even more closely visible when hyperspectral data cubes of Adventdalen[1] are studied in more detail. The view of Adventdalen as captured by the camera of a mobile phone is shown in figure 4.8. In figure 4.9 and 4.10 images constructed using a hyperspectral datacube imaging Adventdalen created on 26-08-2019 at 13:37 have been used. From now on, this datacube will be referred to as datacube L. Again, the grass shows clearly emission in the NIR region of the spectrum.

A hyperspectral datacube recorded two weeks later on 09-09-2019 14:10, from now on referred to as datacube M, shows the same effects. Images reconstructed from this data cube are shown in figures 4.11 and 4.12. Again, the emission of grass in the NIR is clearly visible. Furthermore, when the irradiance of the snow covered mountains in the background is studied in more detail, the irradiance spectrum in

[1]This is a valley to the south-east of Longyearbyen.

Figure 4.5: Image generated from hyperspectral datacube K recorded on 26-08-2019 13:14. The wavelengths used for the RGB image are: red 780 nm, green 540 nm and blue 480 nm.

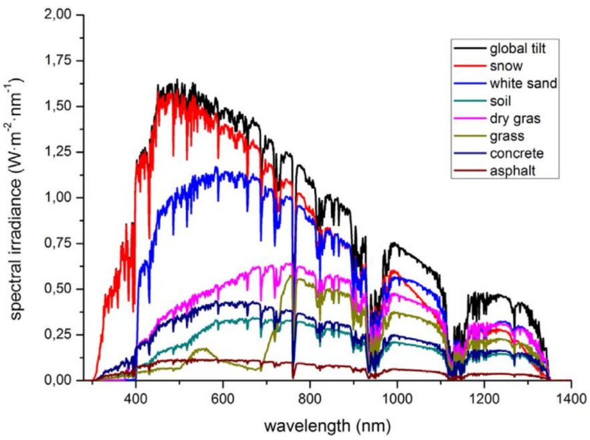

Figure 4.6: Albedo irradiance spectra for different ground components. The black line represents the solar spectral irradiance. The image is retrieved from [27].

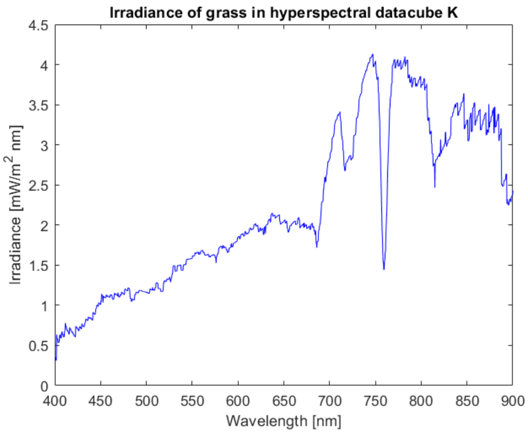

Figure 4.7: The irradiance spectrum of a grass covered part of hyperspectral datacube K.

figure 4.13 is found. It can be seen that this irradiance spectrum is indeed comparable to that of the Albedo spectrum of snow found by A. Fillipo as seen in figure 4.6.

Figure 4.8: Mobile phone picture of Adventdalen taken from the roof of UNIS on 09-09-2019 14:40.

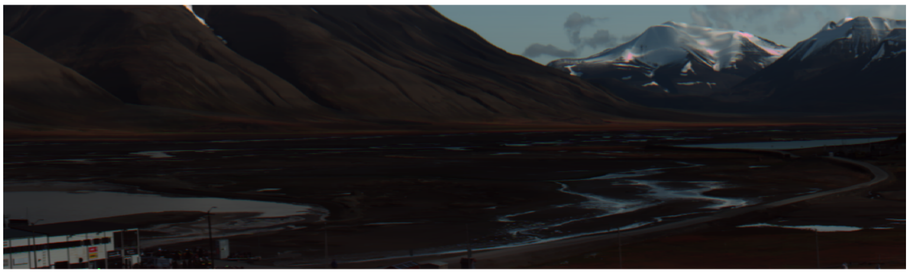

Figure 4.9: Image generated from hyperspectral datacube L recorded on 26-08-2019 13:37. The wavelengths used for the RGB image are: red 660 nm, green 540 nm and blue 480 nm.

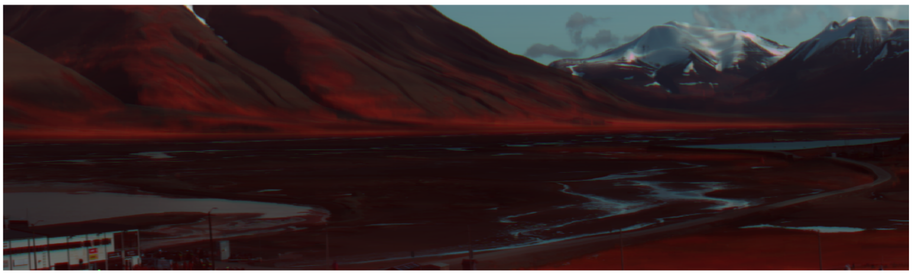

Figure 4.10: Image generated from hyperspectral datacube L recorded on 26-08-2019 13:37. The wavelengths used for the RGB image are: red 780 nm, green 540 nm and blue 480 nm.

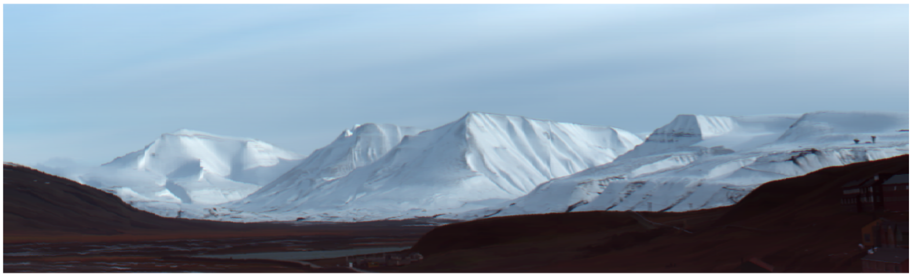

Figure 4.11: Image generated from hyperspectral datacube M recorded on 09-09-2019 14:10. The wavelengths used for the RGB image are: red 660 nm, green 540 nm and blue 480 nm.

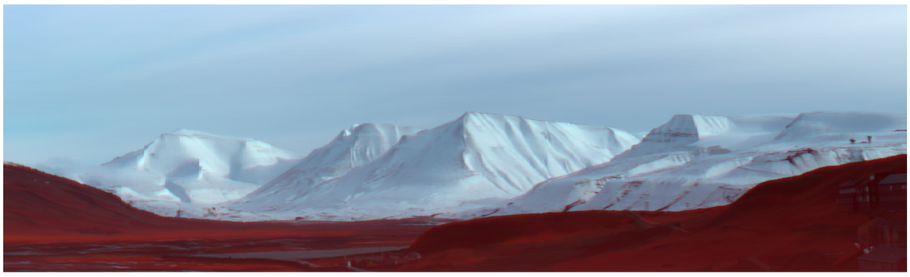

Figure 4.12: Image generated from hyperspectral datacube M recorded on 09-09-2019 14:10. The wavelengths used for the RGB image are: red 780 nm, green 540 nm and blue 480 nm.

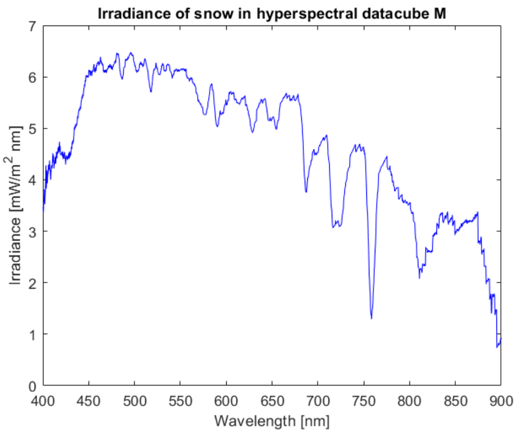

Figure 4.13: Irradiance spectrum of the snow covered mountains in the background from hyperspectral datacube M.

5 Conclusions

The aim of this project was to obtain the spectral signature of the HSI v6 to make the device ready for use in the HYPSO project. This is done by performing several calibration and characterization steps using the centerline of the device. After performing the wavelength and radiometric calibration and characterizing the bandpass, gain function, temporal linearity of the sensor and the second-order diffraction effects, the obtained results are incorporated into the “PlaySpectrogram” program. Therefore, it has been made possible to process recorded data easier now. Thus, the device is ready for use in the HYPSO mission. There are still some further optimization steps possible which will be discussed in Chapter 6.

During the wavelength calibration, it was found that the wavelength range is approximately 270 - 1000 nm. When the efficiency of the different optical elements is taken into account, the usable wavelength range is reduced to 400 - 900 nm. The radiometric calibration has provided a dark current of 15 counts independent of the exposure time and a radiometric calibration constant K which varies between $0.1 - 1$ within the usable wavelength range. It should be noted that the emission profile of the Tungsten lamp used for this radiometric calibration differs a lot from the emission spectrum of the Sun. Therefore, the radiometric calibration might not be performed optimal for outdoor use of the HSI v6. Thus, it would be better to use a calibration lamp with an emission spectrum closer to the spectrum of the Sun.

During the characterization of the HSI v6 an average spectral bandpass of 4 ± 1 nm has been found which is within the theoretical bandpass of 3.3 nm. Furthermore, it has been shown that the gain function is applicable, making it possible to calculate the irradiance without gain when gain has been used during the measurement. Additionally, the temporal sensor response proved to be linear. Lastly, the second-order diffraction effect has been quantified and a formula to compensate for this effect has been found.

Ultimately, this project delivers a proof of functionality that shows that the HSI v6 is able to identify targets and thus is ready for use in the HYPSO project.

6 Further Optimizations and Outlook

Now that the basic functions of the device are working, it would be interesting to look into some further optimizations. First two possibilities for optimization are given in section 6.1 after which some additional ideas for future improvements are discussed in section 6.2.

6.1 Further Optimizations

When processing the data obtained with the HSI v6, an inconsistency in wavelength calibration over several days was found. Additionally, an improvement in the second-order diffraction compensation was found. Both effects will be discussed below.

6.1.1 Inconsistency in Wavelength Calibration

After the wavelength calibration had been performed, an inconsistency in this calibration was discovered. It was found when a calibration check was performed using the location of the Fraunhofer peaks in the solar spectrum for some of the images taken of the surroundings of UNIS. It appeared that the Fraunhofer peaks did not correspond to the proper wavelengths at which these lines should appear. After that new spectral calibration images were taken in the lab and in these images also a wavelength inconsistency was found. The maximum absolute shift that has been observed was 13 pixels. This corresponds to a shift of approximately 5 nm. It is not a shift in one direction, but it shifts up and down when measurements of different days are compared. Therefore, for all the recorded hyperspectral datacubes a wavelength check has been done using the Fraunhofer lines as described in Chapter 4.

This wavelength shift can arise in the HSI v6 device itself and/or in the software. When considering the HSI v6, the 3D printed parts of the HSI could be the origin of the shift. Either the grating is not sufficiently fixed by the 3D printed parts and can be slightly moved when the device shakes or moves. Another possibility is that the heating of the detector when it is connected with the laptop causes the 3D printed part that holds the detector to expand or shrink and therefore slightly moves the detector. In literature, changes in the spectral response parameters due to vibrations or temperature differences have also been reported by Zhao *et al.* [20]. However, these changes were reported due to in-flight circumstances.

To test the hypothesis about the possible moving grating, measurements have been performed. In between the measurements the HSI has been shaken. This did not result in an observable pixel shift. To test whether the heating of the detector and therefore the heating of the 3D printed parts plays a role, image sets with one and two hours in between have been recorded. When there was no measurement, the HSI remained connected with the laptop to ensure that the detector was heated. However, this experiment did not lead to a notable variation of pixel position of the Fraunhofer lines. Therefore, there are no direct indications that the 3D printed parts are the cause of the shift. However, more research is needed to confirm this and if it is possible, it would be better to replace the plastic 3D printed parts by another material that is more stress resistant such as metal or invar materials.

For the storage of videos and images, the IC Capture 2.4 software is used. More specifically, the Xvid MPEG-4 Codec with the Xvid Home profile is used as compression method to store the videos. The wavelength and radiometric calibration images are stored without compression. The Xvid compression decreases the size of the videos by only storing the changes in a frame instead of the entire frame. In this way, the amount of lost information is limited and the size of a two minute video shrinks from over 1 GB to approximately 20 MB. However, when playing a compressed video it seems like the emission lines are shifting a bit in the horizontal direction. This indicates that the exact spectral resolution is partly lost in this method of compression.

However, it should be noted that the wavelength inconsistency also exists in the calibration images which have been stored without compression. Therefore, the compression method cannot be the only source of the wavelength inconsistency. Furthermore, for the calibration the average of multiple calibration images is used in order to exclude the pixel variations in the software.

To study the effect of the compression method in more detail, videos of a fluorescent tube have been recorded using various compression methods. The compression profiles used are Xvid Home, MPEG ASP L0, MPEG ASP L1, MPEG ASP L2, MPEG ASP L3, MPEG ASP L4 and MPEG ASP L5. These profiles are all part of the Xvid MPEG-4 Codec package. For each video, the intensity spectra of frame $2 - 11$ have been plotted on top of each other. To see the differences of the various frames, a zoomed in graph for all the different compression methods has been made of the local minimum between spectral pixels 500 - 540. All the figures can be found in Appendix E. Specifically, the entire spectrum can be found in figure E.1. The zoomed in spectra are found in figures E.2 - E.9.

It can be seen that all compression methods make the spectra coarser, resulting in flat peaks rather than the sharp peaks visible in the non compressed video. For these flat peaks, it is harder to determine the exact center of each peak. Furthermore, for all compression methods, there can be a shift of a few pixels for the starting point of a flat peak. However, it should be noticed that the peaks from the non compressed video are also shifting around a bit.

Therefore, from this small experiment, it cannot be concluded that the compression method used in this project had a severe impact on the wavelength inconsistency. Especially when the fact that all calibration images have been stored without compression has been taken into account. For future studies, it can be good to look more closely at the effect of compression to choose an optimal compression method.

Consequences of this spectral shift are that for each image, a unique wavelength calibration should be performed. This is not only time consuming, but it also makes it hard to perform the radiometric calibration. In principle, the wavelength calibration should be known before performing the radiometric calibration. When the wavelength calibration is slightly different during both the calibration steps, the wavelength range of the particular image will deviate slightly from the range during the radiometric calibration. This deviation makes it hard to multiply the intensity spectra of an image with the radiometric calibration factor K.

Therefore, for the version of the HSI that will be mounted to the student satellite, no plastic 3D printed parts should be used. All these parts should be replaced by metal components to eliminate shrinkage or expansion of the parts due to heating of the detector.

6.1.2 Second-Order Diffraction Effects

When figures 3.12 and 3.14 are compared, it can be noted that in figure 3.12 a small bump between 800 and 900 nm remains, while some the values above 900 nm become negative and are thus set to zero. Therefore, the hypothesis arises that the second-order correction is slightly dependent on the circumstances outside and in particular on the position of the Sun.

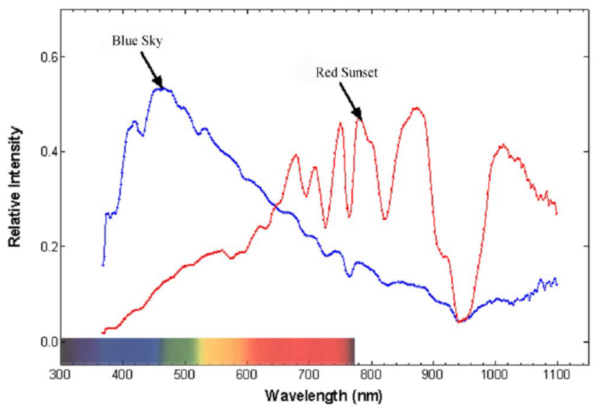

Figure 6.1: The solar spectrum for both a blue sky and a red sunset. The image is taken from [28].

The measurements involving the cut-off filter have been performed in the second half of October in Longyearbyen, while the images from the roof of UNIS have been taken on a beautiful day in August. In the second half of October, the Sun barely rises above the horizon in Longyearbyen. Therefore, the rays have to travel through a greater thickness of the atmosphere before reaching the earth. Since scattering of light in the atmosphere scales with λ^{-4} most of the blue part of the solar spectrum has already scattered before reaching the detector. Thus the resulting solar spectrum has shifted towards the orange and red side [28]. The difference in the solar spectrum for a blue sky and for a red sunset is shown in figure 6.1. It can be seen that for the red sunset, much more absorption peaks due to absorption by water vapor, oxygen and ozone are visible [28].

This effect is for example visible in hyperspectral datacube M recorded at 09-09-2019. When a red wavelength in the NIR of 860 nm is used to generate an image, it is expected that only the parts of Adventdalen covered in grass will appear red in the image. However, in this case, also the sky looks red as shown in figure 6.2.

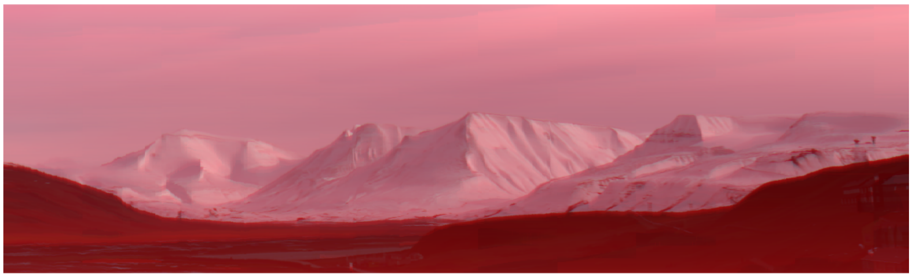

Figure 6.2: Image generated from hyperspectral datacube M recorded on 09-09-2019 14:10. The wavelengths used for the RGB image are: red 860 nm, green 540 nm and blue 480 nm.

Therefore, to obtain a more accurate second-order correction, calibration images using the cut-off filter should be taken for various positions of the Sun to obtain the second-order diffraction efficiency for several positions of the Sun. Subsequently, also the Sun positions of the images taken outside should be registered in order to match these images with the correct second-order diffraction efficiency.

6.2 Outlook

Besides the possible optimizations for the inconsistency in wavelength calibration and the second-order diffraction compensation, some interesting improvements for future work exist as well. To improve the radiometric calibration, it would be good to use a radiometric calibration lamp with an emission spectrum more similar to the solar spectrum, since the device is designed to take image outside with the solar spectrum as a light source. Additionally, to have reliable spectral signatures from objects not in the centerline of the device, the effect of spectral and spatial aberrations should be studied. In case there is a severe effect on the image quality, these abberations should be characterized to eliminate them in the future. Finally, to ensure a good in-flight performance of the HSI, an in-flight calibration should be performed. Afterwards, testing of the device using a drone could give valuable information to ensure a sufficient quality of images taken in-flight.

References

[1] Mariusz E. Grøtte. Ntnu smallsat a hyper-spectral imaging mission, 2018. URL https://www.ntnu.edu/documents/20587845/1277298890/022_Gr%C2%A2tte_NTNU_SmallSat_Mission.pdf/f98477c2-4fb3-4fa9-a01d-d732c93b53a6. last visited: 2019-11-06.

[2] NTNU. Hyper spectral imager for oceanographic applications, . URL https://www.ntnu.edu/ie/smallsat/mission-hyper-spectral-camera. last visited: 2019-11-06.

[3] NTNU. Hyperspectral remote sensing cubesat, . URL https://www.hypso.space/. last visited: 2019-11-25.

[4] F. Vasefi, N. MacKinnon, and D.L. Farkas. Chapter 16 - hyperspectral and multispectral imaging in dermatology. In M. R. Hamblin, P. Avci, and G. K. Gupta, editors, *Imaging in Dermatology*, pages 187 – 201. Academic Press, Boston, 2016. ISBN 978-0-12-802838-4. doi: https://doi.org/10.1016/B978-0-12-802838-4.00016-9. URL http://www.sciencedirect.com/science/article/pii/B9780128028384000169.

[5] L.. Gao and R. T. Smith. Optical hyperspectral imaging in microscopy and spectroscopy – a review of data acquisition. *Journal of Biophotonics*, 8(6):441–456, 2015. doi: 10.1002/jbio.201400051. URL https://onlinelibrary.wiley.com/doi/abs/10.1002/jbio.201400051.

[6] R. Lu and B. Park. *Introduction*, pages 3–7. Springer New York, New York, NY, 2015. ISBN 978-1-4939-2836-1. doi: 10.1007/978-1-4939-2836-1_1. URL https://doi.org/10.1007/978-1-4939-2836-1_1.

[7] A. F. H. Goetz. Three decades of hyperspectral remote sensing of the earth: A personal view. *Remote Sensing of Environment*, 113:S5 – S16, 2009. ISSN 0034-4257. doi: https://doi.org/10.1016/j.rse.2007.12.014. URL http://www.sciencedirect.com/science/article/pii/S003442570900073X. Imaging Spectroscopy Special Issue.

[8] Khan H. S. Yousaf A. Khurshid K. Khan, M. J. and A. Abbas. Modern trends in hyperspectral image analysis: A review. *IEEE Access*, 6:14118–14129, 2018. doi: 10.1109/ACCESS.2018.2812999.

[9] Goetz A. F. H. Vane, G. and J. B. Wellman. Airborne imaging spectrometer: A new tool for remote sensing. *IEEE Transactions on Geoscience and Remote Sensing*, GE-22(6):546–549, Nov 1984. doi: 10.1109/TGRS.1984.6499168.

[10] Syrjäsuo M. Storvold R. Fortuna J. Eivind Grøtte M. Sigernes, F. and T. Arne Johansen. Do it yourself hyperspectral imager for handheld to airborne operations. *Opt. Express*, 26(5):6021–6035, Mar 2018. doi: 10.1364/OE.26.006021. URL http://www.opticsexpress.org/abstract.cfm?URI=oe-26-5-6021.

[11] M. Bøe Henriksen. Hyperspectral imager calibration and image correction. Master's thesis, Norwegian University of Science and Technology, Norway, 2019.

[12] Dimitris G. Manolakis, Ronald B. Lockwood, and Thomas W. Cooley. *Hyperspectral Imaging Remote Sensing: Physics, Sensors, and Algorithms.* Cambridge University Press, 2016. doi: 10.1017/CBO9781316017876.

[13] F. Sigernes. Basic hyper spectral imaging, ttk20: Hyperspectral remote sensing - detailed lecture notes, 2018.

[14] Cbuckley. Creative commons attribution-share alike 3.0. URL https://commons.wikimedia.org/w/index.php?curid=1911215. last visited: 2019-10-25.

[15] L. Que, C. Wilson, and Y. Gianchandani. Microfluidic electrodischarge devices with integrated dispersion optics for spectral analysis of water impurities. *Microelectromechanical Systems, Journal of*, 14:185 – 191, 05 2005. doi: 10.1109/JMEMS.2004.839337.

[16] Loewen E. G. Richardson Grating Laboratory. Thermo RGL Palmer, C. A. *Diffraction grating handbook fifth edition.* Rochester, N.Y: Thermo RGL, 2002.

[17] V. Klemas. Remote sensing of algal blooms: An overview with case studies. *Journal of Coastal Research*, 28:34–43, 01 2012. doi: 10.2112/JCOASTRES-D-11-00051.1.

[18] D. Bruna. Nijntje. URL https://www.ixxiyourworld.com/nl/producten/ixxi-images/nijntje06/. last visited: 2019-11-26.

[19] Sun Y. Fang A. Qi W. Yu, X. and C. Liu. Laboratory spectral calibration and radiometric calibration of hyper-spectral imaging spectrometer. In *The 2014 2nd International Conference on Systems and Informatics (ICSAI 2014)*, pages 871–875, Nov 2014. doi: 10.1109/ICSAI.2014.7009407.

[20] Geng R. Jia G. Zhao, H. and D. Wang. Uncertainty analysis of in-flight spectral calibration for hyperspectral imaging spectrometers. In Lorenzo Bruzzone, editor, *Image and Signal Processing for Remote Sensing XXIII*, volume 10427, pages 123 – 131. International Society for Optics and Photonics, SPIE, 2017. doi: 10.1117/12.2277702. URL https://doi.org/10.1117/12.2277702.

[21] Holmes J. M. Dyrland M. Lorentzen D. A. Chernous S. A. Svinyu T. Moen J. Sigernes, F. and C. S. Deehr. Absolute calibration of optical devices with a small field of view. *J. Opt. Technol.*, 74(10): 669–674, Oct 2007. doi: 10.1364/JOT.74.000669. URL http://jot.osa.org/abstract.cfm?URI=jot-74-10-669.

[22] Jia G. Yuan Y. Tao, D. and H. Zhao. A digital sensor simulator of the pushbroom offner hyperspectral imaging spectrometer. *Sensors*, 14(12):23822–23842, 2014. ISSN 1424-8220. doi: 10.3390/s141223822. URL https://www.mdpi.com/1424-8220/14/12/23822.

[23] Huw Fox and Bill Bolton. 1 - functions. In H. Fox and B. Bolton, editors, *Mathematics for Engineers and Technologists*, IIE Core Textbooks Series, pages 1 – 56. Butterworth-Heinemann, Oxford, 2002. ISBN 978-0-7506-5544-6. doi: https://doi.org/10.1016/B978-075065544-6/50002-3. URL http://www.sciencedirect.com/science/article/pii/B9780750655446500023.

[24] Miyamura N. Yokoya, N. and A. Iwasaki. Preprocessing of hyperspectral imagery with consideration of smile and keystone properties. *Proceedings of SPIE - The International Society for Optical Engineering*, 7857, 10 2010. doi: 10.1117/12.870437.

[25] M. Veisdal J. Honore-Livermore E. Fortuna J. Prentice E. F. Syrjäsuo M. Rajan K. Sigernes F., Eivind Grøtte and T. Arne Johansen. Pushbroom hyper spectral imager version 6 (hsi v6) part list - final prototype. 2018.

[26] Cebula R. P. Huang, L. K. and E. Hilsenrath. New procedure for interpolating NIST FEL lamp irradiances. *Metrologia*, 35(4):381–386, aug 1998. doi: 10.1088/0026-1394/35/4/27. URL https://doi.org/10.1088%2F0026-1394%2F35%2F4%2F27.

[27] F. Annoni. *Progress in photovoltaic cells based on Low-Temperature Pulsed-Electron-Deposited Cu(In,Ga)Se2 films*. PhD thesis, 03 2017.

[28] G. Rechtsteiner and J. Ganske. Using natural and artificial light sources to illustrate quantum mechanical concepts. *The Chemical Educator*, 3:1–12, 08 1998. doi: 10.1007/s00897980230a.

[29] Edmund optics #49-579, 2019. URL https://www.edmundoptics.com/p/300-grooves-25mm-sq-175deg-blaze-angle-grating/10092/. last visited: 2019-10-02.

[30] DMK 33UX174 Monochrome Camera, 2017. URL https://www.1vision.co.il/pdfs/The_imaging_source/Datasheet/fsdmk33ux174.en_US.pdf/. last visited: 2019-10-02.

Appendix

A Typical Calibration Errors

During both the wavelength and the radiometric calibration, initially some errors were made. In order to avoid such errors in future calibration studies of a HSI, a list of those errors have been made.

Typical calibration errors with corresponding advice:

- First control if all emission lines appear at exactly the same wavelength at all times. In case of this project, only in a later stadium it was discovered that this was not the case. Knowing this earlier in the process can help to avoid a lot of frustration.
- Try to use a spectral lamp with a spectrum as close as possible to the solar spectrum to avoid having to compensate for second-order diffraction effects present in the HSI device.
- When trying to obtain the same result in two different programs (in my case Matlab and PlaySpectrogram), try to check if all the parameters are used in the same way. Differences I encountered where:
  - Matlab starts counting at 1 for all kind of arrays and matrices, while programs like Python and PlaySpectrogram start counting at 0. In this project, this lead to a mismatch of obtained parameters.
  - Matlab counts the pixels starting at the top, while PlaySpectrogram starts at the bottom. So when trying to get information about the point spectrum of one pixel, this difference should be taken into account just as the difference in starting point for counting (0 versus 1).
  - Carefully check the number of frames, because this might be different for different programs. For this specific project, the videos are recorded by IC Capture 2.4. In IC Capture 2.4, a value for Frames per Second (FPS) can be chosen. Theoretically, IC Capture 2.4 should store a number of frames equal to fps · duration video. However, to reduce the size of the video files, a compression is used and therefore only the changes in pixels for all the different frames are stored. This means that only a new frame is stored when the image has changed, meaning that the exposure time in combination with the time it takes to save an image will be the limiting factor. Hence, less frames than fps · duration video are stored when the exposure time and the time it takes to save an image are larger than 1/FPS. Since the time it takes to store an image is not defined, it differs depending on how much of the processor of the computer is used. Therefore, the number of frames stored by IC Capture 2.4 can not always be predicted. However, it can help to give the program IC Capture 2.4 priority to use the processor of the laptop.

    Matlab (the .NumberOfFrames property of VideoReader) reads the actual number of frames which IC Capture 2.4 stores. However, PlaySpectrogram calculates the number of frames using FPS · duration video. This makes it hard to produce the point spectrum of exactly the same pixel in both programs.

B Efficiency Curves of Transmission Grating and Detector

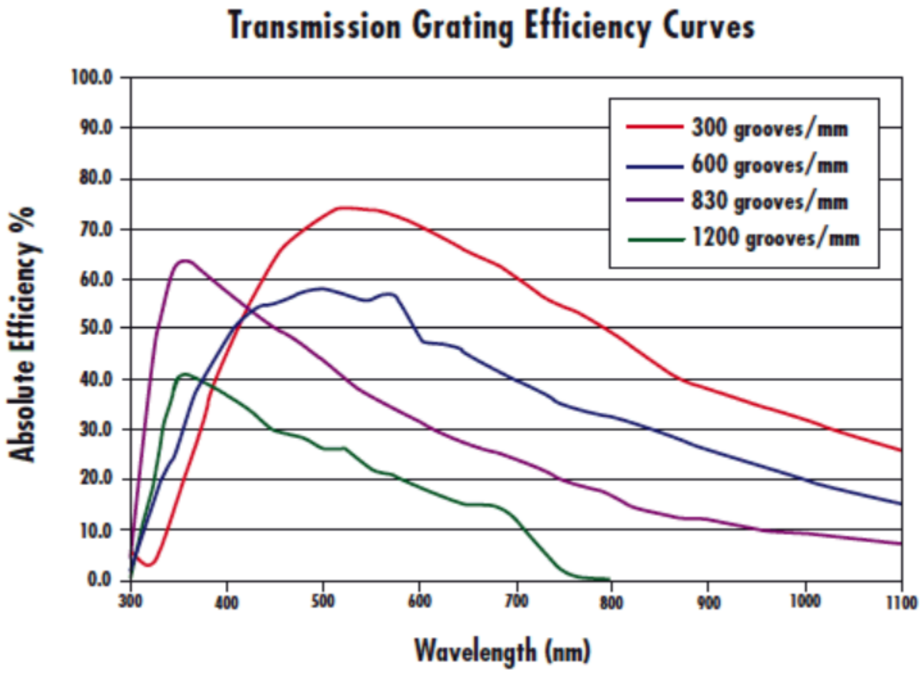

Figure B.1: The transmission grating efficiency curves showing the absolute efficiency [%] as a function of the wavelength. The grating used in this project is the 300 grooves/mm grating.[29]

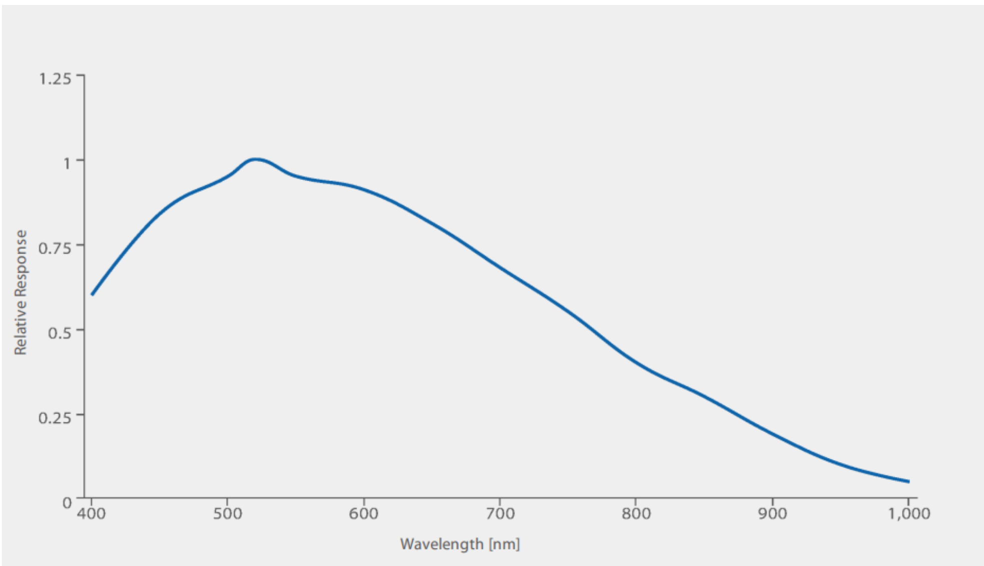

Figure B.2: The spectral response curve of the Sony IMX174LL sensor which is incorporated in the DMK33UX174 camera head.[30]

C Calibration Certificate 1000 W Tungsten Lamp

63350-M
QUARTZ TUNGSTEN HALOGEN LAMP STANDARDS
OF SPECTRAL IRRADIANCE: 1kW, 200 W, 45 W

CALIBRATION RESULTS

Wattage : 1000 W
Model No. : 63350
Serial No. : XXXXX
Spectral Range : 250-2400 nm
Lamp Current : 8.2 Amps
Voltage : 110.6 Volts
Room Temp : 27.0°C
Date : September 1, 1995

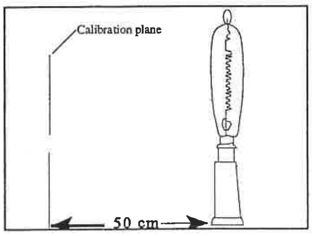

DIRECTLY MEASURED IRRADIANCE VALUES

Wavelength (nm)	Spectral Irradiance (uW/cm^2 -nm)	Spectral Wavelength (nm)	Irradiance (uW/cm^2 -nm)
250.0	1.670E-2	555.0	9.945E0
260.0	2.980E-2	600.0	1.258E1
270.0	4.930E-2	654.6	1.533E1
280.0	7.760E-2	700.0	1.736E1
290.0	1.170E-1	800.0	2.057E1
300.0	1.708E-1	900.0	2.134E1
310.0	2.351E-1	1050.0	2.022E1
320.0	3.307E-1	1150.0	1.856E1
330.0	4.416E-1	1200.0	1.766E1
340.0	5.790E-1	1300.0	1.580E1
350.0	7.374E-1	1540.0	1.156E1
360.0	9.369E-1	1600.0	1.076E1
370.0	1.161E0	1700.0	9.288E0
380.0	1.415E0	2000.0	6.197E0
390.0	1.696E0	2100.0	5.480E0
400.0	2.016E0	2300.0	4.178E0
450.0	3.731E0	2400.0	3.651E0
500.0	6.725E0		

13

INTERPOLATED IRRADIANCE VALUES

Wavelength (nm)	Spectral Irradiance (uW/cm^2 -nm)	Wavelength (nm)	Spectral Irradiance (uW/cm^2 -nm)	Wavelength (nm)	Spectral Irradiance (uW/cm^2 -nm)
250.0	1.670E-2	720.0	1.800E1	1190.0	1.784E1
260.0	2.980E-2	730.0	1.832E1	1200.0	1.766E1
270.0	4.930E-2	740.0	1.864E1	1210.0	1.747E1
280.0	7.760E-2	750.0	1.896E1	1220.0	1.729E1
290.0	1.170E-1	760.0	1.928E1	1230.0	1.710E1
300.0	1.708E-1	770.0	1.960E1	1240.0	1.692E1
310.0	2.351E-1	780.0	1.993E1	1250.0	1.673E1
320.0	3.307E-1	790.0	2.025E1	1260.0	1.655E1
330.0	4.416E-1	800.0	2.057E1	1270.0	1.636E1
340.0	5.790E-1	810.0	2.064E1	1280.0	1.617E1
350.0	7.374E-1	820.0	2.072E1	1290.0	1.599E1
360.0	9.369E-1	830.0	2.080E1	1300.0	1.580E1
370.0	1.161E0	840.0	2.088E1	1310.0	1.563E1
380.0	1.415E0	850.0	2.095E1	1320.0	1.545E1
390.0	1.696E0	860.0	2.103E1	1330.0	1.527E1
400.0	2.016E0	870.0	2.111E1	1340.0	1.510E1
410.0	2.359E0	880.0	2.119E1	1350.0	1.492E1
420.0	2.702E0	890.0	2.126E1	1360.0	1.474E1
430.0	3.045E0	900.0	2.134E1	1370.0	1.457E1
440.0	3.388E0	910.0	2.126E1	1380.0	1.439E1
450.0	3.731E0	920.0	2.119E1	1390.0	1.421E1
460.0	4.330E0	930.0	2.111E1	1400.0	1.404E1
470.0	4.929E0	940.0	2.104E1	1410.0	1.386E1
480.0	5.528E0	950.0	2.096E1	1420.0	1.368E1
490.0	6.127E0	960.0	2.089E1	1430.0	1.351E1
500.0	6.725E0	970.0	2.082E1	1440.0	1.333E1
510.0	7.311E0	980.0	2.074E1	1450.0	1.315E1
520.0	7.896E0	990.0	2.067E1	1460.0	1.298E1
530.0	8.482E0	1000.0	2.059E1	1470.0	1.280E1
540.0	9.067E0	1010.0	2.052E1	1480.0	1.262E1
550.0	9.653E0	1020.0	2.044E1	1490.0	1.245E1
560.0	1.024E1	1030.0	2.037E1	1500.0	1.227E1
570.0	1.082E1	1040.0	2.029E1	1510.0	1.209E1
580.0	1.141E1	1050.0	2.022E1	1520.0	1.192E1
590.0	1.200E1	1060.0	2.005E1	1530.0	1.174E1
600.0	1.258E1	1070.0	1.988E1	1540.0	1.156E1
610.0	1.308E1	1080.0	1.972E1	1550.0	1.143E1
620.0	1.359E1	1090.0	1.955E1	1560.0	1.129E1
630.0	1.409E1	1100.0	1.939E1	1570.0	1.116E1
640.0	1.459E1	1110.0	1.922E1	1580.0	1.103E1
650.0	1.510E1	1120.0	1.906E1	1590.0	1.089E1
660.0	1.557E1	1130.0	1.889E1	1600.0	1.076E1
670.0	1.602E1	1140.0	1.873E1	1610.0	1.061E1
680.0	1.646E1	1150.0	1.856E1	1620.0	1.047E1
690.0	1.691E1	1160.0	1.838E1	1630.0	1.032E1
700.0	1.736E1	1170.0	1.820E1	1640.0	1.017E1
710.0	1.768E1	1180.0	1.802E1	1650.0	1.002E1

Wavelength (nm)	Spectral Irradiance (uW/cm^2-nm)
1660.0	9.877E0
1670.0	9.730E0
1680.0	9.582E0
1690.0	9.435E0
1700.0	9.288E0
1710.0	9.185E0
1720.0	9.082E0
1730.0	8.979E0
1740.0	8.876E0
1750.0	8.773E0
1760.0	8.670E0
1770.0	8.567E0
1780.0	8.464E0
1790.0	8.361E0
1800.0	8.258E0
1810.0	8.155E0
1820.0	8.052E0
1830.0	7.949E0
1840.0	7.846E0
1850.0	7.743E0
1860.0	7.640E0
1870.0	7.537E0
1880.0	7.434E0
1890.0	7.331E0
1900.0	7.228E0
1910.0	7.125E0
1920.0	7.022E0
1930.0	6.919E0
1940.0	6.816E0
1950.0	6.713E0
1960.0	6.610E0
1970.0	6.506E0
1980.0	6.403E0
1990.0	6.300E0
2000.0	6.197E0
2010.0	6.126E0
2020.0	6.054E0
2030.0	5.982E0
2040.0	5.910E0
2050.0	5.839E0
2060.0	5.767E0
2070.0	5.695E0
2080.0	5.623E0
2090.0	5.551E0
2100.0	5.480E0
2110.0	5.415E0
2120.0	5.350E0
2130.0	5.284E0
2140.0	5.219E0
2150.0	5.154E0
2160.0	5.089E0

Wavelength (nm)	Spectral Irradiance (uW/cm^2-nm)
2170.0	5.024E0
2180.0	4.959E0
2190.0	4.894E0
2200.0	4.829E0
2210.0	4.764E0
2220.0	4.699E0
2230.0	4.634E0
2240.0	4.569E0
2250.0	4.504E0
2260.0	4.439E0
2270.0	4.374E0
2280.0	4.308E0
2290.0	4.243E0
2300.0	4.178E0
2310.0	4.126E0
2320.0	4.073E0
2330.0	4.020E0
2340.0	3.968E0
2350.0	3.915E0
2360.0	3.862E0
2370.0	3.809E0
2380.0	3.757E0
2390.0	3.704E0
2400.0	3.651E0

D Transmission Graph Sharp Cut Red Filters

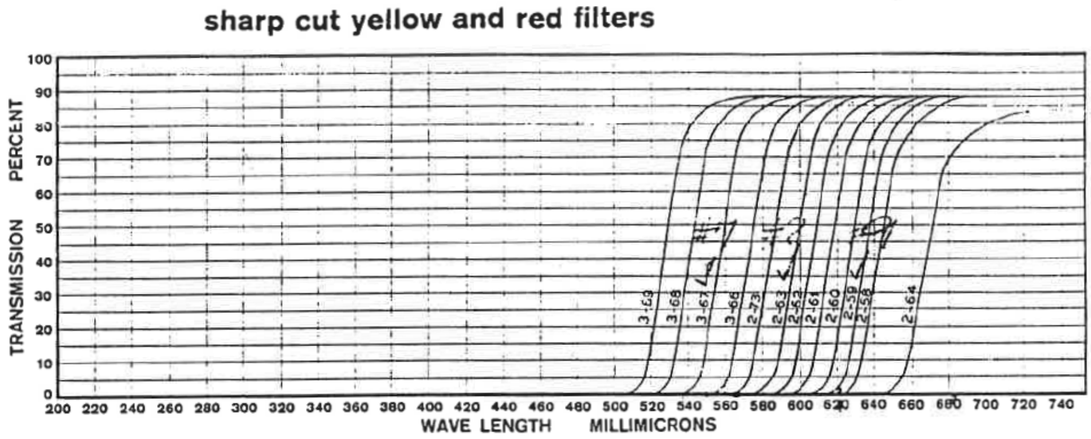

Figure D.1: The transmission percentage for different red cut off filters as a function of wavelength.

E Different Compression Techniques

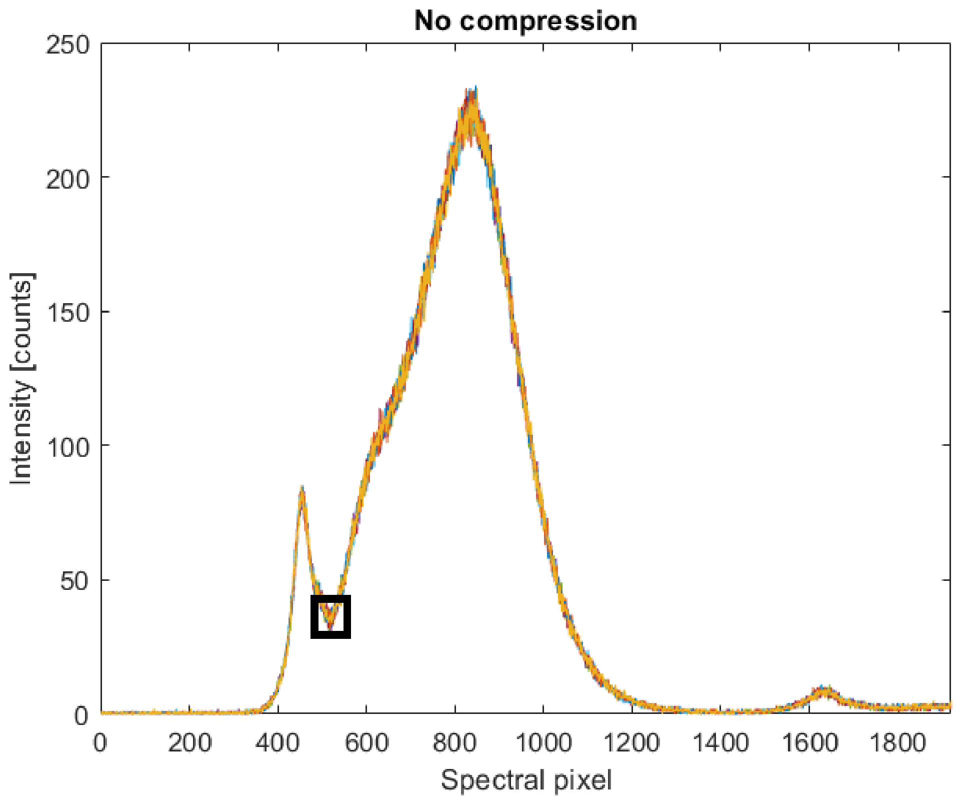

Figure E.1: The intensity spectra of frames 2 - 11 of a video taken from a fluorescent tube without compression.

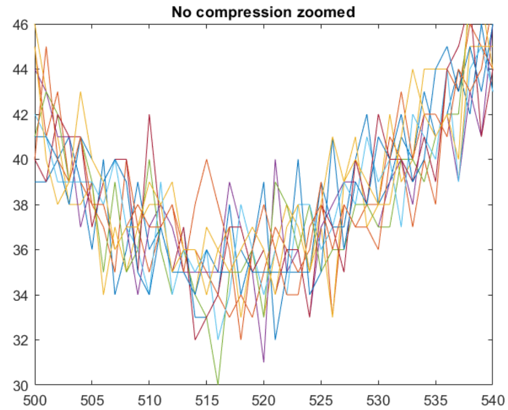

Figure E.2: Zoomed in on the one absorbance peak in the intensity spectra of frames 2 - 11 from a non compressed video from a fluorescent tube. The black box represents the area at which is zoomed in for the following images.

Figure E.3: Zoomed in on the one absorbance peak in the intensity spectra of frames 2 - 11 from a video with xvid home compression from a fluorescent tube.

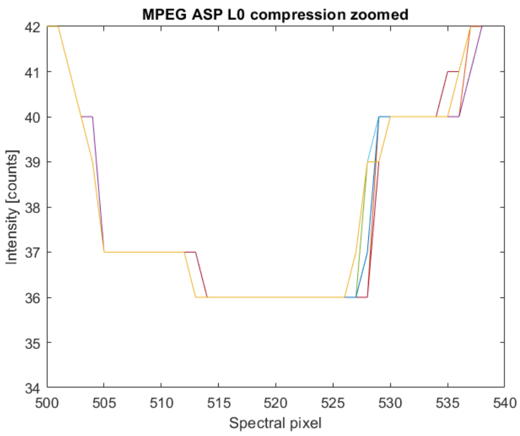

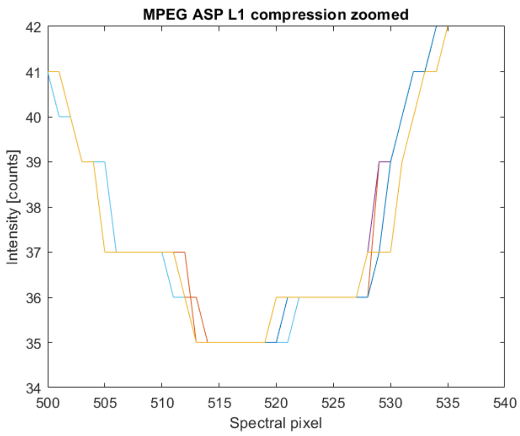

Figure E.4: Zoomed in on the one absorbance peak in the intensity spectra of frames 2 - 11 from a video with MPEG ASP L0 compression from a fluorescent tube.

Figure E.5: Zoomed in on the one absorbance peak in the intensity spectra of frames 2 - 11 from a video with MPEG ASP L1 compression from a fluorescent tube.

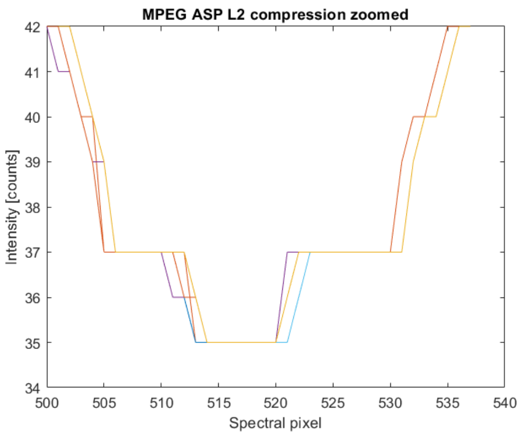

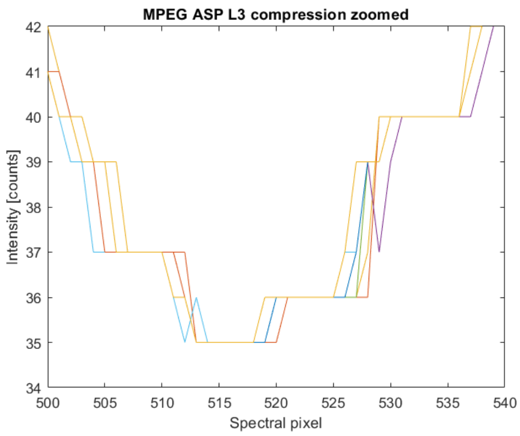

Figure E.6: Zoomed in on the one absorbance peak in the intensity spectra of frames 2 - 11 from a video with MPEG ASP L2 compression from a fluorescent tube.

Figure E.7: Zoomed in on the one absorbance peak in the intensity spectra of frames 2 - 11 from a video with MPEG ASP L3 compression from a fluorescent tube.

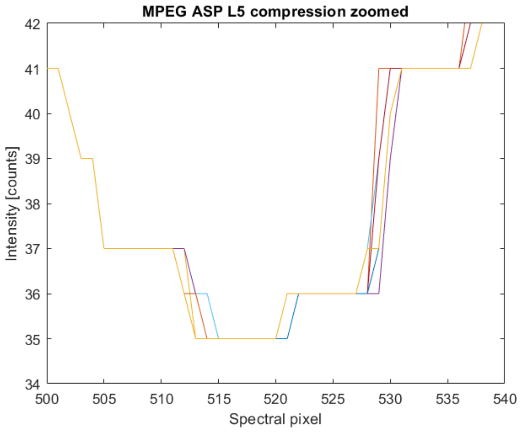

Figure E.8: Zoomed in on the one absorbance peak in the intensity spectra of frames 2 - 11 from a video with MPEG ASP L5 compression from a fluorescent tube.

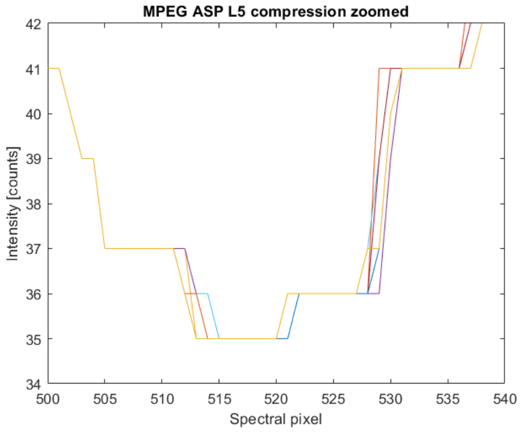

Figure E.9: Zoomed in on the one absorbance peak in the intensity spectra of frames 2 - 11 from a video with MPEG ASP L5 compression from a fluorescent tube.